


## Article

# Geochronology and Geochemical Characteristics of Granitoids in the Lesser Xing'an–Zhangguangcai Range: Petrogenesis and Implications for the Early Jurassic Tectonic Evolution of the Mudanjiang Ocean

Jingui Kong <sup>1</sup>, Kai Qiao <sup>2,\*</sup> , Xiaoyu Huo <sup>3</sup>, Guobin Zhang <sup>4</sup>, Xingkai Chen <sup>5</sup> and Lei Yao <sup>1</sup><sup>1</sup> Shandong Provincial Nuclear Industry Geological Group 273, Yantai 264000, China; kjg@163.com (J.K.)<sup>2</sup> Civil-Military Integration Center of China Geological Survey, Chengdu 610036, China<sup>3</sup> Qingdao Geo-Engineering Surveying Institute, Qingdao 266000, China; ffyy7280@163.com<sup>4</sup> Department of Earth Science and Engineering, Shanxi Institute of Engineering Technology, Yangquan 045000, China; zhangguobin85@163.com<sup>5</sup> Jiangsu Coal Geological Survey Team, Nanjing 210000, China; chxingkai@163.com

\* Correspondence: qk6173@126.com



**Citation:** Kong, J.; Qiao, K.; Huo, X.; Zhang, G.; Chen, X.; Yao, L. Geochronology and Geochemical Characteristics of Granitoids in the Lesser Xing'an–Zhangguangcai Range: Petrogenesis and Implications for the Early Jurassic Tectonic Evolution of the Mudanjiang Ocean. *Minerals* **2024**, *14*, 941. <https://doi.org/10.3390/min14090941>

Academic Editors: José Francisco Molina, Yunsheng Ren and Qun Yang

Received: 26 July 2024

Revised: 2 September 2024

Accepted: 12 September 2024

Published: 15 September 2024

**Correction Statement:** This article has been republished with a minor change. The change does not affect the scientific content of the article and further details are available within the backmatter of the website version of this article.



**Copyright:** © 2024 by the authors. Licensee MDPI, Basel, Switzerland. This article is an open access article distributed under the terms and conditions of the Creative Commons Attribution (CC BY) license (<https://creativecommons.org/licenses/by/4.0/>).

**Abstract:** This article focuses on zircon U-Pb isotope dating and a whole-rock elemental analysis of granodiorites, monzonitic granites, granodioritic porphyries, and alkali feldspar granites in the Yangmugang area of the Lesser Xing'an–Zhangguangcai Range. The zircon U-Pb isotope-dating results revealed that these granitic rocks formed during the late Early Jurassic period (182.9–177.2 Ma). Their geochemical characteristics and zircon saturation temperatures suggest that the granodiorites are moderately differentiated I-type granites and the monzonitic granite, granodioritic porphyries, and alkali feldspar granites are highly differentiated I-type granites. The degree of magma differentiation progressively increased from granodiorites to alkali feldspar granites. By combining the regional Nd and Hf isotope compositions, it was inferred that the magma source involved the melting of lower crustal material from the Mesoproterozoic to the Neoproterozoic eras. By integrating these findings with contemporaneous intrusive rock spatial variations, it was indicated that the late Early Jurassic granitoids in the Lesser Xing'an–Zhangguangcai Range formed within an extensional tectonic setting after the collision and closure of the Songnen–Zhangguangcai Range and Jiamusi blocks. Additionally, this study constrains the closure of the Mudanjiang Ocean to the late Early Jurassic period (177.2 Ma).

**Keywords:** Lesser Xing'an–Zhangguangcai Range; Early Jurassic; I-type granitoids; zircon U-Pb age; petrogeochemistry; magmatic evolution; Mudanjiang Ocean

## 1. Introduction

The Lesser Xing'an–Zhangguangcai Range is situated at the junction of the eastern segment of the Central Asian Orogenic Belt, the northern segment of the North China Craton, and the ancient Pacific tectonic system [1,2]. During the Paleozoic to Early Mesozoic periods, it was influenced and controlled by the ancient Asian oceanic tectonic system, characterized by the collision and amalgamation of multiple micro-continental blocks [3–6]. During the Mesozoic era, the region underwent superimposed modifications from the Paleo-Pacific tectonic system, characterized by extension following composite continental collision [7–9]. This led to intense tectonic and magmatic activity in the area, with the widespread development of Mesozoic magmatic rocks and a complex variety of rock types. This constitutes an important component of the Mesozoic “large granite province” at the eastern margin of the East Asian continent [10]. Previous studies have indicated that this region hosts a significant amount of trending Phanerozoic magmatic rocks and sporadic exposures of Late Paleozoic strata [11,12]. In recent years, a large number of zircon U-Pb dating results have shown that the Phanerozoic magmatic rocks in the Lesser Xing'an–Zhangguangcai

Range mainly formed during the Late Paleozoic to Early Mesozoic periods, with a smaller amount forming during the Neoproterozoic and Early Paleozoic periods [13–15]. These Late Paleozoic to Early Mesozoic medium-acidic rock assemblages primarily consist of quartz diorite, granodiorite, monzonitic granite, syenitic granite, and a small amount of alkaline feldspar granite. They belong to the medium-K–high-K calc-alkaline series, with a decreasing  $P_2O_5$  content as the  $SiO_2$  content increases [6,8,11] and an  $A/CNK < 1.1$  [12], indicating a peraluminous to weakly peraluminous granite [14]. They exhibit the characteristics of I-type granites [11,14], and during the emplacement process, they underwent an extended fractional crystallization process [16,17]. The Sr–Nd isotopes and zircon Lu–Hf isotopes indicate that these Early to Middle Mesozoic granites are components of a juvenile continental crust, recording the crustal accretion process during the Phanerozoic period in the Central Asian Orogenic Belt [18,19]. However, there has been ongoing controversy regarding the tectonic setting in which the Early to Middle Mesozoic magmatic rocks in the Lesser Xing’an–Zhangguangcai Range formed, primarily encompassing the following four viewpoints: (1) The magmatic activity in this region occurred in an extensional environment, resulting from the decompression melting caused by the post-collisional delamination of the Xing’an–Mongolia Orogenic Belt and the North China Craton [4,20]. (2) The magmatic rocks formed in a post-subduction extensional environment related to the westward subduction of the ancient Pacific Ocean [21,22]. (3) The magmatic rocks were generated in an extensional tectonic setting, under the combined control of the Mongolia–Okhotsk oceanic tectonic system and the Paleo-Pacific tectonic system [23,24]. (4) The Lesser Xing’an–Zhangguangcai Range was situated within a subduction environment and represented a continental margin magmatic arc formed during the westward subduction of the Mudanjiang Ocean [11,12,25–27]. Together with the blueschist of Heilongjiang on the eastern side, it constitutes an arc-trench system [28]. The Yangmugang area is located in the southern segment of the Lesser Xing’an–Zhangguangcai Range, with an extensive distribution of magmatic rocks within the region. It holds indicative significance for studying the Mesozoic tectonic and magmatic activities in the northeastern region of China. Accordingly, the present study conducted detailed field geological investigations, selecting granitic rocks from the Yangmugang area for zircon U–Pb geochronology, a lithofacies analysis, and whole-rock geochemical research in order to determine their formation age and petrogenesis. At the same time, by comprehensively analyzing the existing geological data of Early to Middle Mesozoic intrusive rocks in the Lesser Xing’an–Zhangguangcai Range, a comprehensive exploration of the tectonic environment during the Early to Middle Mesozoic period was conducted.

## 2. Geological Settings and Samples

### 2.1. Geological Background

The Lesser Xing’an–Zhangguangcai Range is located in the northern part of the Xingmeng Orogenic Belt, situated between the North China Craton and the Siberian Craton [1]. From the Paleozoic to the Early Mesozoic periods, this region formed a tectonic stack due to the collision and amalgamation of multiple micro-continents, accretionary terranes, and tectonic belts. These micro-continents are divided from west to east into the Erguna block, the Xing’an block, the Songnen–Zhangguangcai Range block, the Jiamusi block, and the Khanka block [3–5,8]. The western part of the Songnen–Zhangguangcai Range block, where the study area is located, features younger sediments from the Late Mesozoic to the Cenozoic periods in the Songliao Basin [29]. The eastern part is divided into the Lesser Xing’an–Zhangguangcai Range tectonic belt by the north–south-trending Jiamusi–Yilan Fault [2]. This region exhibits sporadic outcrops of Paleozoic volcanic–sedimentary strata and metamorphic marine sedimentary strata, with the extensive development of Middle to Late Mesozoic volcanic–sedimentary formations and Phanerozoic granites [21,25,29]. To the east of the study area, the Jiamusi block is a micro-continent with an ancient crystalline basement, connected to the Songnen–Zhangguangcai Range block via the Heilongjiang Complex. The magmatic activity in this block has been concentrated in four periods [11]:

the Cambrian, Permian, Triassic, and Cretaceous periods. The amalgamation history of the Songnen–Zhangguangcai Range block and the Jiamusi block—two crucial tectonic units at the eastern end of the Xingmeng Orogenic Belt—is closely related to the evolution of the Mudanjiang Ocean, with the Mudanjiang Suture Zone serving as the boundary between the Songnen–Zhangguangcai Range block and the Jiamusi block [25]. The Heilongjiang Complex, a key piece of evidence for the evolution of the Mudanjiang Ocean, forms a north–south-trending belt distributed in the Luobei–Jiayin, Yilan–Huanan, and Mudanjiang areas of Heilongjiang Province [11,15,30]. It primarily consists of blueschists, serpentinites, amphibolites, greenschists, phengite schists, and marbles. Its petrological and geochemical characteristics indicate that the protolith of the blueschists has an oceanic island basalt nature and was formed during the Permian–Triassic period, with metamorphism occurring in the Late Triassic–Jurassic period [11,27]. Therefore, the Heilongjiang Complex is considered a high-pressure metamorphic belt formed by the subduction, collision, and amalgamation between the Songnen–Zhangguangcai Range block and the Jiamusi block [11,28].

The investigated area is located in the eastern segment of the Central Asian Orogenic Belt (Figure 1a), to the east of the Songliao Basin and to the west of the Jiamusi–Yilan Fault Zone, in the Zhangguangcai Range. The tectonic position of the area belongs to the uplifted belt of the Lesser Xing’an Range–Songnen block (Figure 1b). The exposed strata in the investigated area encompass a range from the Paleozoic to the Cenozoic eras. The Paleozoic strata consist of the Middle Permian Tumenling Formation ( $P_2t$ ). The Mesozoic strata comprise the Upper Jurassic Mao’ershan Formation ( $J_3ms$ ) and the Lower Cretaceous Ningyuancun Formation ( $K_1n$ ). The Cenozoic strata encompass the Paleogene Baoquanling Formation (Eb), the Neogene Harbin Formation ( $Qp^3h$ ), and the Quaternary Lower Man Tan Deposits ( $Qh^{al}$ ) (Figure 1c). The Middle Permian Tumenling Formation ( $P_2t$ ) sporadically outcrops in the northwestern part of the surveyed area, exhibiting an irregular north–south-oriented distribution. The lithology primarily consists of lithic sandstone, mudstone, and fine–medium-grained lithic feldspathic sandstone. The Upper Jurassic Hatuoshan Formation ( $J_3ms$ ) is extensively distributed in the southern part of the surveyed area, sporadically outcropping in the central and northern parts. It exhibits an irregular northeast-oriented distribution pattern, representing a monoclinical geological structure. The predominant rock types include gray-white flow-banded rock, flow-banded volcanic ash with angular lithic fragments, and granite. The Lower Cretaceous Ninyuan Village Formation ( $K_1n$ ) is primarily distributed in the eastern part of the surveyed area, exhibiting an irregular northward extension. It represents a monoclinical geological structure. The predominant rock types consist of gray-purple and purple-red flow-banded volcanic ash with angular lithic fragment conglomerates and andesitic welded tuff. The Gujianshan Formation (Eb) of the Paleogene System sporadically occurs in the lower terrain of the northwestern part of the surveyed area. It displays an irregular pattern with gentle dips. The predominant rock types include gray-white and gray-green conglomeratic coarse sandstone, conglomeratic medium sandstone, siltstone, silty mudstone, and mudstone. The Quaternary Harbin Formation ( $Qp^3h$ ) is distributed in the northwestern part of the surveyed area in an irregular pattern. The predominant rock types consist of grayish subclay and gray-yellow loess-like subclay. The Quaternary Holocene Alluvial Deposits ( $Qh^{al}$ ) are widely distributed in the study area. The predominant rock types include yellow-brown subclay, yellow conglomeratic medium–coarse sand, and a sand–gravel mixture. In the study area, intrusive rocks are developed, primarily consisting of Jurassic granitoids, with a minor amount of Late Paleozoic granites. The rock types include granodiorite, monzonitic granite, granitic porphyry, and alkali feldspar granite. The study area exhibits both brittle and ductile structural features, with brittle fractures predominantly trending in the northwest and near east–west directions. These fractures display characteristics of multiple phases of activity. The northwest-trending fractures intersect Early Jurassic alkaline granite and Early Jurassic diorite.

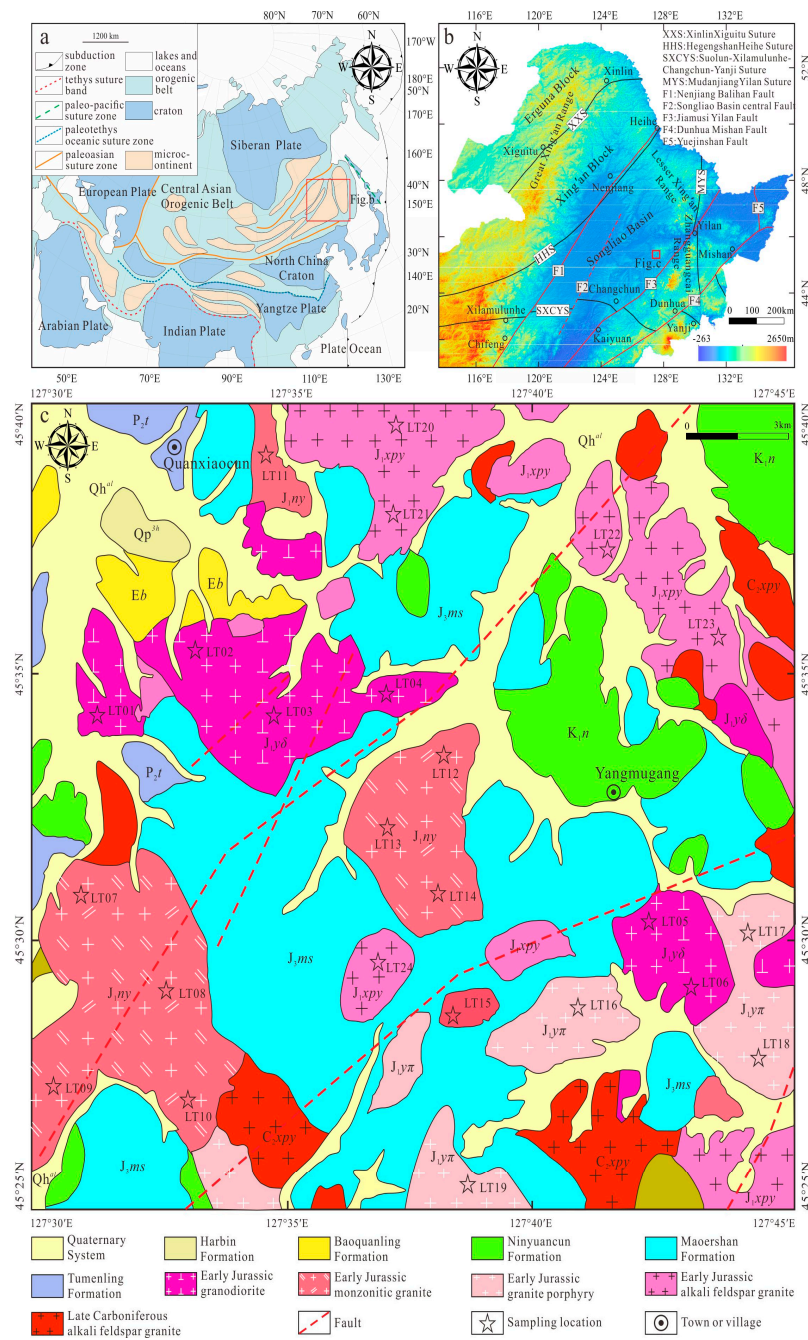


**Figure 1.** Schematic tectonic map showing the main subdivisions of Central and East Asia (a) (modified from [31]); the tectonic divisions of NE China, showing the major blocks, sutures, and faults (b) (modified from [12,32]); and a geological map of the study area (c).

### 2.2. Petrological Characteristics

Early Jurassic intrusive rocks in the Yangmugang area of the Lesser Xing’an–Zhangguangcai Range are widely distributed in the study area. Early Jurassic granodiorite is primarily exposed in the central part of the study area, with the rock body trending east–west and comprising four intrusive bodies covering an approximate area of 50.45 Km<sup>2</sup>. These bodies are unconformably overlain by Hatuoshan Formation flow-banded rocks and weathered surfaces are observable at the contact zones. Early Jurassic monzonitic granite is mainly exposed in the southwestern part of the study area, trending north–south and comprising four intrusive bodies covering an approximate area of 68.30 Km<sup>2</sup>. Early Jurassic granitic porphyry sporadically occurs in the study area, with the exposure of five intrusive bodies

covering an approximate area of 28.75 Km<sup>2</sup>. Early Jurassic alkali feldspar granite is primarily exposed in the northeastern part of the study area, covering an approximate area of 56.70 Km<sup>2</sup>.

The weathered surface of the granodiorite is grayish brown and the fresh surface is grayish white, with a medium–fine-grained granite structure, and the joints are relatively developed (Figure 2a,b). Microscopic observations showed that the main mineral composition includes alkali feldspar (30–32 vol%), plagioclase (40–43 vol%), quartz (17–20 vol%), biotite (3 vol%), and a small amount of accessory minerals, including hornblende (2 vol%) (Figure 2f). The alkali feldspar displays a subhedral to tabular morphology with a graphic texture. The crystals are mostly wrapped with fine particles such as plagioclase and quartz. A few of them are sericitized and become turbid, the quartz is in an allotriomorphic granular shape, and the biotite is in a flaky crystal shape.

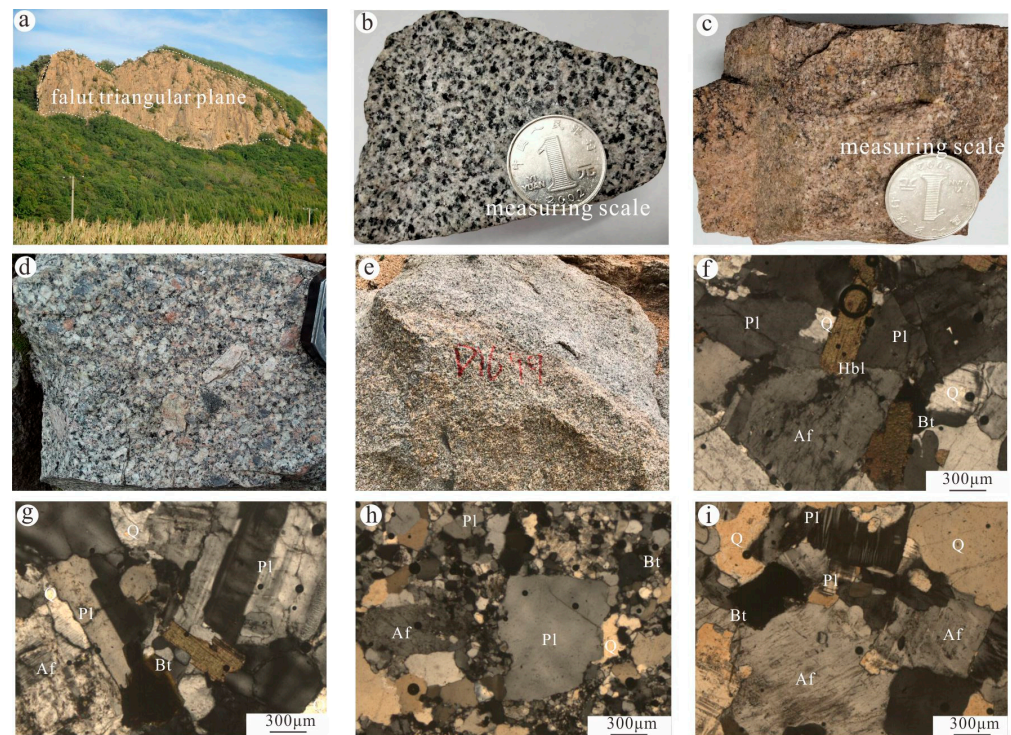


**Figure 2.** Field and microscopic photos of Early Jurassic granitoids from the Yangmugang area in Lesser Xing’an–Zhangguangcai Range. (a) macroscopic outcrop of monzogranite; (b) hand specimens of granodiorite (sample Lt02); (c) hand specimens of monzogranite (sample Lt08); (d) monzogranite granitic porphyry (sample Lt16); and (e) hand specimens of alkali feldspar granite (sample Lt21); (f) granodiorite microscopic characteristics; (g) monzogranite microscopic characteristics; (h) granitic porphyry microscopic characteristics; (i) alkali feldspar granite microscopic characteristics (sample LT21). Q-quartz; Pl-plagioclase; Af-alkali feldspar; Bt-biotite; Hbl-hornblende.

The weathered surface of the monzogranite is grayish brown, and the fresh surface is a light flesh red, with a medium–fine-grained granite structure (Figure 2c). Microscopic observations showed that the main mineral composition is alkali feldspar (27–30 vol%), plagioclase (36–39 vol%), quartz (25–29 vol%), and biotite (1%) (Figure 2g). The alkali feldspar is in a semi-automorphic plate shape, with microcline and perthite varieties, and it exhibits a graphic texture with quartz. The plagioclase is in a semi-automorphic plate shape with a zoning texture, and polysynthetic twinning can be seen. The quartz is in an anhedral term shape with varying sizes. The biotite is in a brown flaky shape, with a particle size of 0.15–0.6 mm.

The granitic porphyry is gray-red with phenocrysts and a hypidiomorphic granular texture; the matrix has a finely crystalline texture (Figure 2d) and is composed of alkali

feldspar (29–32 vol%), plagioclase (37–40 vol%), quartz (24–27 vol%), and biotite (1 vol%) (Figure 2h). The alkali feldspar appears as xenomorphic granular shapes with a striped texture and grain sizes of approximately 0.8–2.8 mm. The plagioclase feldspar displays a subhedral tabular morphology with visible twinning. The quartz appears as an anhedral term shape. In some areas, it shows graphic intergrowth with alkali feldspar, distributed within interstitial spaces. The biotite is brown in color and exhibits flaky crystal forms. There are small amounts of accessory minerals such as zircon.

The alkali feldspar granite is flesh-red (Figure 2e) with a medium-to-fine massive granitic structure composed of alkali feldspar (54–58 vol%), plagioclase (14–16 vol%), quartz (20–24 vol%), and biotite (1 vol%) along with accessory minerals, including apatite and magnetite (1 vol%) (Figure 2i). The alkali feldspar exhibits a subhedral tabular morphology with a striped texture, and a small portion of it has undergone sericitization. The plagioclase feldspar displays a subhedral tabular morphology with zoning structures. The quartz appears as xenomorphic granular shapes, often occurring in aggregates. The biotite is brown in color and exhibits flaky crystal forms.

### 3. Samples and Analytical Methods

A total of 24 zircon U-Pb isotope-dating samples and rock geochemical samples were collected in this study. The zircon U-Pb isotope-dating sample LT02 and 6 rock geochemical samples (LT01-LT06) were collected from the Early Jurassic granodiorite. Dating samples LT08 and 9 rock geochemical samples (LT07-LT15) were collected from the Early Jurassic monzonitic granite. Dating sample LT16 and 4 rock geochemical samples (LT16-LT19) were collected from the Early Jurassic granodioritic porphyries. Dating sample LT21 and 5 rock geochemical samples (LT20-LT24) were collected from the Early Jurassic alkali feldspar granite.

#### 3.1. Zircon U-Pb Dating

The zircon samples were mechanically crushed to an 80–100 mesh and, after flotation and electromagnetic separation and using a binocular microscope, representative single zircon crystals with a complete crystal morphology, good transparency, and fewer fractures and inclusions were selected for dating purposes. The preparation of zircon thin sections, the cathodoluminescence image acquisition, and the isotope analysis were conducted at the State Key Laboratory of Continental Dynamics at Northwest University. Data testing was performed using the ComPex102 ArF excimer laser (wavelength of 193 nm) produced by Coherent Lambda Physik and the Agilent 7500a ICP-MS instrument with a Shield Torch produced by Agilent, Niedersachsen, Germany. The working material was ArF, the diameter of the laser beam spot was 30  $\mu\text{m}$ , and the depth of the laser ablation sample was 20–40  $\mu\text{m}$ . High-purity helium gas was used as the carrier gas for ablation and the instrument optimization was conducted using the artificially synthesized silicate material SRM610, developed by the National Institute of Standards and Technology (NIST) in the United States. The Harvard University zircon standard 91,500 ( $^{206}\text{Pb}/^{238}\text{U} = 1065.4 \pm 0.6 \text{ Ma}$ ) was used for the calibration of isotopic fractionation and mass discrimination effects during the ablation [33], transportation, and ionization processes. ICP-MS DataCal was employed for data processing [34]. The calculation of the age-weighted mean and the construction of Concordia plots for dating data were accomplished using the Isoplot 4.0 software [35].

#### 3.2. Whole-Rock Major and Trace Element Analysis

The rock geochemical sample testing and analyses were carried out at the Harbin Mineral Resources Supervision and Testing Center of the Ministry of Natural Resources. Major elements were analyzed using the glass bead X-ray fluorescence spectroscopy (XRF) method. First, 0.60 g of powdered sample was weighed and placed in a small porcelain crucible that had been preheated to a constant weight. Then, the crucible was placed in a muffle furnace preheated to around 1000  $^{\circ}\text{C}$  and ignited for 60 min. After the crucible was removed and allowed to cool to room temperature, it was weighed again and the loss on

ignition (LOI) of the sample was calculated. Next, the measured sample powder was mixed with 4 g of  $\text{Li}_2\text{B}_4\text{O}_7$  flux and placed on a fusion machine, then heated to approximately 1060 °C to melt it into a homogeneous glass disk within a gold crucible. After the sample cooled, X-ray fluorescence (XRF) (Zetium produced by Panalytical, Almelo, Netherlands) was used to test it, achieving an analytical accuracy and precision better than 5%. Trace element and rare earth element analyses were conducted using ICP-MS. Firstly, 200-mesh powdered samples were weighed and placed into a polytetrafluoroethylene digestion vessel. A solution of HF and  $\text{HNO}_3$  was added, and the high-pressure digestion vessel was maintained at 190 °C for 72 h in a drying oven. After removal, the sample was diluted with hydrochloric acid to a specified volume and placed into the instrument for analysis. The precision and accuracy of the analysis were better than 5%, and the analysis error for certain volatile elements and elements with extremely low concentrations was better than 10%.

## 4. Analysis Results

### 4.1. Zircon U-Pb Geochronology

The LA-ICP-MS zircon U-Pb isotope analysis test data of the granitoid samples from the Yangmugang area of the Lesser Xing'an–Zhangguangcai Range from the Early Jurassic period are shown in Table 1.

Sample LT02 was collected from the granodiorite within 10 km to the east of Yangmugang. The coordinates of the sampling point were 45°34'05" N, 127°34'25" E. The zircon grains were euhedral to subhedral elongated prismatic crystals, with an elongated axis of 150–250  $\mu\text{m}$  and length/width ratios of 1.5:1–2:1. In the CL images, the zircon grains exhibited distinct magmatic oscillatory zoning (Figure 3), and the Th/U values of 25 measuring points ranged from 0.21 to 1.90 (>0.1), indicating a typical magmatic origin for the zircons [36]. The age values for all the measurement points of sample LT02 were located on or near the Concordia curve (Figure 4a), indicating a good concordance (individual zircon concordance > 85%). The weighted average age of the 25 zircon grains was  $182.9 \pm 1.4$  Ma (MSWD = 0.5), representing the crystallization age.

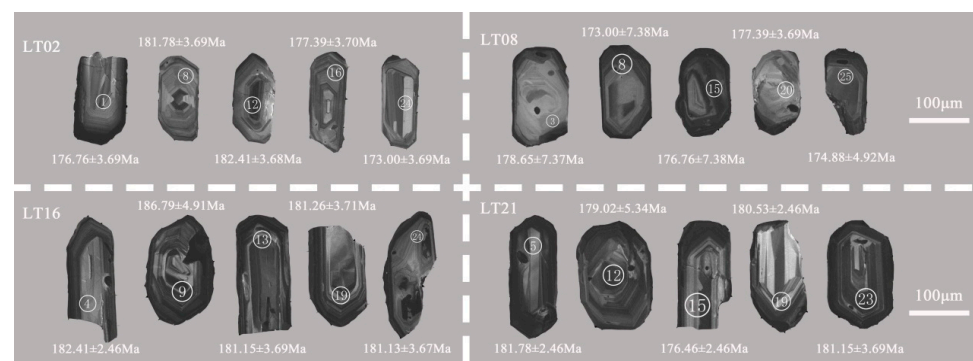


**Figure 3.** Typical zircon cathodoluminescence images of Late Jurassic granite from the Yangmugang area in the Lesser Xing'an–Zhangguangcai Range. The white circles denote laser spots.

Sample LT08 was collected from the monzonitic granite located 15 km to the southeast of Yangmugang. The coordinates of the sampling point were 45°29'03" N, 127°32'45" E. The zircon grains were euhedral to subhedral elongated prismatic crystals, with an elongated axis of 110–150  $\mu\text{m}$  and length/width ratios of 1:1–1.5:1. In the CL images, the zircon grains exhibited distinct magmatic oscillatory zoning (Figure 3), and the Th/U values of 25 measuring points ranged from 0.45 to 0.95 (>0.1), indicating a typical magmatic origin for the zircons [36]. Excluding the 3 zircon grains with poor concordance (LT21-01, LT21-18, LT21-21), the remaining 22 zircon grains were situated on or near the Concordia curve (Figure 4b). The weighted average age of 21 zircon grains was  $180.8 \pm 0.9$  Ma (MSWD = 0.3), representing the crystallization age. Additionally, one zircon grain had an age of  $318.20 \pm 9.62$  Ma, which was considered a detrital zircon age.

**Table 1.** Zircon U-Pb isotopic date for Early Jurassic granitoids from Yangmugang area in the Lesser Xing'an-Zhanguangcai Range.

Spot No	Content (ppm)			Isotopic Ratios								Isotopic Ages (Ma)						Concordance (%)		
	Pb	U	Th	<sup>206</sup> Pb/ <sup>238</sup> U	1σ	<sup>207</sup> Pb/ <sup>235</sup> U	1σ	<sup>207</sup> Pb/ <sup>206</sup> Pb	1σ	<sup>208</sup> Pb/ <sup>232</sup> Th	1σ	<sup>232</sup> Th/ <sup>238</sup> U	1σ	<sup>206</sup> Pb/ <sup>238</sup> U	1σ	<sup>207</sup> Pb/ <sup>235</sup> U	1σ		<sup>207</sup> Pb/ <sup>206</sup> Pb	1σ
Lt02-01	17.14	498.32	758.29	0.0288	0.0003	0.2006	0.003	0.0503	0.0006	0.0109	0.0001	0.7837	0.01	183.03	3.68	185.63	4.97	207.84	54.21	98.58
Lt02-02	3.13	91.76	153.64	0.0287	0.0006	0.2169	0.0172	0.0544	0.0041	0.0155	0.0007	0.3631	0.0013	182.41	7.37	199.33	28.13	386.64	331.75	90.72
Lt02-03	14.13	381.23	633.28	0.0288	0.0002	0.2176	0.0039	0.0546	0.0008	0.0116	0.0002	0.6995	0.0072	183.03	2.46	199.91	6.37	394.87	64.40	90.78
Lt02-04	12.15	439.61	614.29	0.0287	0.0002	0.2103	0.0046	0.0532	0.0011	0.0137	0.0005	0.2659	0.0015	182.41	2.46	193.80	7.56	336.32	91.83	93.76
Lt02-05	9.89	354.78	633.84	0.0287	0.0003	0.2192	0.0054	0.0549	0.0012	0.0111	0.0002	0.7214	0.0051	182.41	3.68	201.24	8.81	407.15	95.87	89.68
Lt02-06	5.96	184.29	352.13	0.0288	0.0003	0.2186	0.0064	0.0553	0.0014	0.0129	0.0002	0.4227	0.0015	183.03	3.68	200.74	10.45	423.37	110.72	90.32
Lt02-07	14.05	367	678.56	0.0287	0.0003	0.2038	0.0031	0.0512	0.0007	0.0116	0.0001	0.3979	0.0053	182.41	3.68	188.34	5.12	248.81	61.68	96.75
Lt02-08	3.98	115.23	211.20	0.0295	0.0004	0.2052	0.0122	0.0506	0.0027	0.0146	0.0007	0.3532	0.0018	187.42	4.91	189.52	20.15	221.61	241.91	98.88
Lt02-09	113.26	287.65	359.67	0.0294	0.0004	0.225	0.0131	0.0564	0.0012	0.0466	0.0003	0.5485	0.0018	186.79	4.91	206.06	21.28	467.15	92.35	89.68
Lt02-10	9.86	307.94	485.76	0.028	0.0003	0.2022	0.0052	0.0505	0.0011	0.0138	0.0003	0.3852	0.0026	178.02	3.69	186.99	8.61	217.03	98.83	94.96
Lt02-11	5.23	165.76	198.56	0.0287	0.0003	0.2187	0.0086	0.0553	0.002	0.0135	0.0006	0.3423	0.0014	182.41	3.68	200.83	14.04	423.37	158.18	89.90
Lt02-12	10.98	326.78	432.76	0.0285	0.0003	0.2072	0.0084	0.0525	0.0018	0.0131	0.0004	0.7336	0.0054	181.15	3.69	191.20	13.85	306.22	153.09	94.45
Lt02-13	9.87	341.23	521.03	0.0285	0.0003	0.2088	0.0046	0.0532	0.0011	0.0115	0.0002	0.4695	0.0062	181.15	3.69	192.55	7.57	336.32	91.83	93.71
Lt02-14	10.12	314.78	213.20	0.0284	0.0003	0.2013	0.0047	0.0511	0.001	0.0118	0.0002	0.5628	0.0058	180.53	3.69	186.23	7.79	244.31	88.36	96.84
Lt02-15	7.94	253.56	378.93	0.0284	0.0003	0.2186	0.0059	0.0556	0.0014	0.0131	0.0004	0.3286	0.0022	180.53	3.69	200.74	9.64	435.43	109.90	88.81
Lt02-16	14.32	424.38	389.76	0.0292	0.0003	0.2143	0.0035	0.0532	0.0008	0.0121	0.0002	0.3851	0.0015	185.54	3.68	197.15	5.74	336.32	66.78	93.74
Lt02-17	3.97	139.78	256.12	0.0284	0.0003	0.2148	0.0098	0.0545	0.0022	0.0145	0.0005	0.3683	0.0015	180.53	3.69	197.57	16.05	390.76	177.56	90.56
Lt02-18	9.24	305.46	287.96	0.0281	0.0004	0.2124	0.0037	0.0547	0.0009	0.0098	0.0001	0.6985	0.0064	178.65	4.92	195.56	6.07	398.97	72.27	90.53
Lt02-19	9.76	325.67	413.69	0.0285	0.0003	0.2091	0.0037	0.0532	0.0009	0.0108	0.0001	0.5353	0.0022	181.26	3.71	192.80	6.09	336.32	75.13	93.57
Lt02-20	7.89	231.35	157.96	0.0293	0.0003	0.2083	0.0085	0.0519	0.0019	0.0164	0.0007	0.3119	0.0015	186.17	3.68	192.13	14.00	279.98	164.23	96.80
Lt02-21	7.32	204.79	175.68	0.0293	0.0003	0.2102	0.0068	0.0524	0.0015	0.0122	0.0002	0.6654	0.0018	186.17	3.68	193.72	11.18	301.88	127.91	95.94
Lt02-22	9.06	284.35	346.53	0.0296	0.0002	0.2193	0.0039	0.0543	0.0009	0.0121	0.0002	0.4038	0.0016	188.04	2.45	201.33	6.37	382.50	73.01	92.93
Lt02-23	16.23	471.32	216.73	0.0287	0.0003	0.2112	0.0057	0.0527	0.0013	0.0127	0.0004	0.7004	0.0313	182.41	3.68	194.56	9.37	314.88	109.97	93.34
Lt02-24	9.32	314.78	265.94	0.0285	0.0003	0.2109	0.0051	0.0533	0.0012	0.0133	0.0005	0.2789	0.0008	181.13	3.67	194.31	8.38	340.57	99.91	92.74
Lt02-25	9.76	301.68	168.79	0.0287	0.0003	0.2185	0.0067	0.0547	0.0014	0.0126	0.0003	0.5716	0.0052	182.41	3.68	200.66	10.94	398.97	112.42	90.00
Lt08-01	8.79	262.79	443.62	0.0283	0.0003	0.3221	0.0208	0.0821	0.0046	0.0109	0.0005	0.6687	0.0032	179.90	3.69	283.52	31.31	1247.02	215.02	96.38
Lt08-02	11.89	368.13	384.76	0.0286	0.0001	0.1964	0.0035	0.0511	0.0008	0.0093	0.0001	0.4807	0.0035	181.78	1.23	182.08	5.82	244.31	70.68	99.83
Lt08-03	17.65	506.23	263.75	0.0287	0.0002	0.1938	0.0041	0.0492	0.0008	0.0104	0.0002	0.3346	0.0023	182.41	2.46	179.87	6.83	156.32	74.60	98.61
Lt08-04	8.78	237.89	158.20	0.0284	0.0003	0.1934	0.0051	0.0492	0.0013	0.0092	0.0001	0.7514	0.0012	180.53	3.69	179.53	8.50	156.32	121.23	99.45
Lt08-05	13.57	348.79	173.28	0.0286	0.0002	0.1963	0.0036	0.0497	0.0011	0.0107	0.0001	0.6095	0.0026	181.78	2.46	181.99	5.99	179.94	101.11	99.88
Lt08-06	16.08	564.03	683.35	0.0285	0.0002	0.1922	0.0034	0.0487	0.0009	0.0105	0.0001	0.8695	0.0101	181.15	2.46	178.50	5.68	132.36	85.17	98.54
Lt08-07	8.79	286.78	324.76	0.0285	0.0001	0.1933	0.0049	0.0492	0.0011	0.0121	0.0003	0.5194	0.0093	181.15	1.23	179.44	8.17	156.32	102.58	99.06
Lt08-08	30.78	678.79	486.37	0.0281	0.0002	0.1907	0.0043	0.0493	0.0011	0.0098	0.0001	0.4025	0.0024	178.65	2.46	177.23	7.19	161.07	102.28	99.21
Lt08-09	12.59	413.79	345.67	0.0283	0.0001	0.1932	0.0029	0.0495	0.0008	0.0104	0.0001	0.5392	0.0027	179.90	1.23	179.36	4.84	170.53	73.96	99.70
Lt08-10	19.86	516.93	321.10	0.0284	0.0002	0.1966	0.0053	0.0505	0.0014	0.0109	0.0003	0.1883	0.0009	180.53	2.46	182.25	8.81	217.03	125.79	99.05
Lt08-11	15.78	405.76	679.34	0.0286	0.0004	0.1954	0.0104	0.0497	0.0012	0.0109	0.0003	0.0627	0.0002	181.78	4.91	181.23	17.31	179.94	110.30	99.70
Lt08-12	15.12	480.95	365.40	0.0284	0.0002	0.1928	0.0032	0.0494	0.0007	0.0081	0.0002	0.7261	0.0052	180.53	2.46	179.02	5.34	165.81	64.90	99.16
Lt08-13	39.89	545.13	162.80	0.0506	0.0008	0.0786	0.0801	0.1541	0.0092	0.0301	0.0021	0.8466	0.0051	318.20	9.62	76.83	147.79	2391.16	199.15	24.15
Lt08-14	13.14	345.69	347.51	0.0284	0.0002	0.1952	0.0064	0.0496	0.0014	0.0091	0.0001	0.9586	0.0062	180.53	2.46	181.06	10.66	175.24	129.05	99.71
Lt08-15	14.32	529.76	875.27	0.0278	0.0002	0.1972	0.0058	0.0512	0.0013	0.0194	0.0007	0.2232	0.0005	176.76	2.46	182.75	9.64	248.81	114.55	96.61
Lt08-16	5.23	194.06	203.65	0.0285	0.0002	0.1967	0.0079	0.0498	0.0018	0.0106	0.0002	0.6122	0.0011	181.15	2.46	182.33	13.14	184.62	164.98	99.35
Lt08-17	34.62	623.15	413.17	0.0283	0.0002	0.1958	0.0015	0.0486	0.0004	0.0107	0.0001	0.2442	0.0016	179.90	2.46	181.57	2.50	127.52	37.96	99.07
Lt08-18	27.06	567.12	403.71	0.0283	0.0001	0.4668	0.0047	0.1191	0.0011	0.0078	0.0002	1.8804	0.0547	179.90	1.23	288.98	6.38	1941.96	32.38	39.36
Lt08-19	20.98	525.78	466.52	0.0284	0.0002	0.1947	0.0052	0.0496	0.0012	0.0125	0.0002	0.6985	0.0087	180.53	2.46	180.63	8.66	175.24	110.62	99.94
Lt08-20	32.16	548.04	452.33	0.0285	0.0002	0.1962	0.0058	0.0497	0.0012	0.0114	0.0002	0.9625	0.0112	181.15	2.46	181.91	9.65	179.94	110.30	99.58
Lt08-21	7.92	320.65	378.14	0.0283	0.0005	0.3241	0.0603	0.0826	0.0197	0.0157	0.0008	0.5988	0.0038	179.90	6.14	285.05	90.63	1258.90	913.74	99.97
Lt08-22	46.78	532.04	502.39	0.0286	0.0002	0.1952	0.0023	0.0496	0.0006	0.0101	0.0001	0.9837	0.0098	181.78	2.46	181.06	3.83	175.24	55.31	99.60
Lt08-23	13.79	421.08	276.53	0.0285	0.0003	0.1949	0.0124	0.0498	0.0031	0.0112	0.0002	0.7986	0.0033	181.15	3.69	180.80	20.65	184.62	284.13	99.81

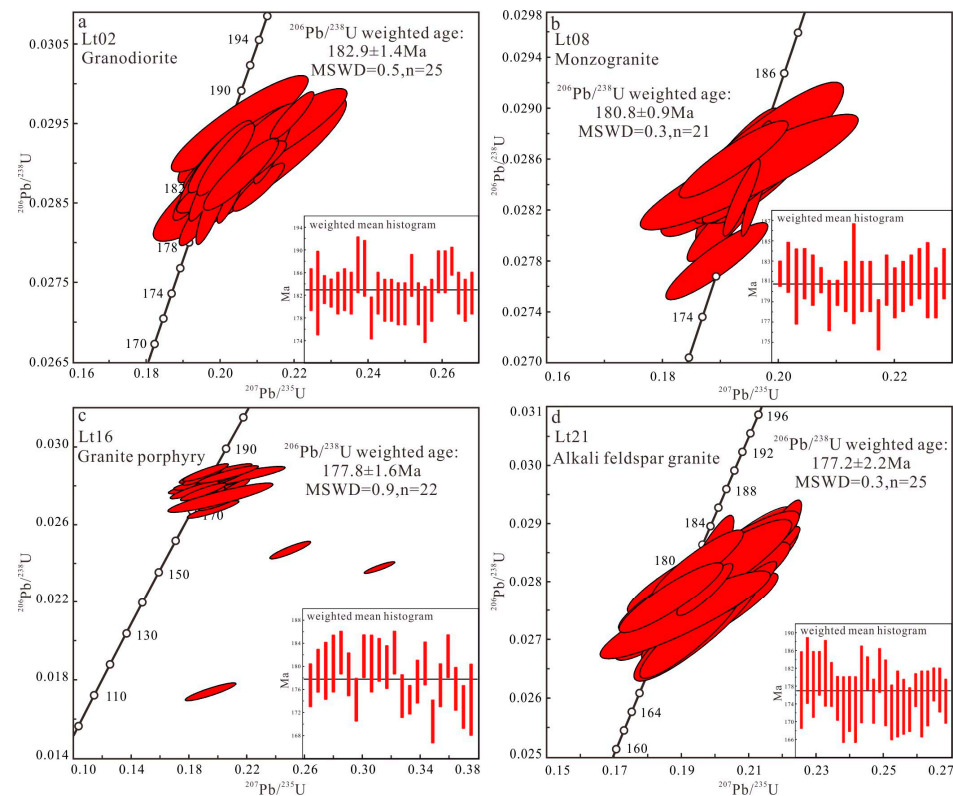


Table 1. Cont.

Spot No	Content (ppm)			Isotopic Ratios								Isotopic Ages (Ma)						Concordance (%)		
	Pb	U	Th	<sup>206</sup> Pb/ <sup>238</sup> U	1σ	<sup>207</sup> Pb/ <sup>235</sup> U	1σ	<sup>207</sup> Pb/ <sup>206</sup> Pb	1σ	<sup>208</sup> Pb/ <sup>232</sup> Th	1σ	<sup>232</sup> Th/ <sup>238</sup> U	1σ	<sup>206</sup> Pb/ <sup>238</sup> U	1σ	<sup>207</sup> Pb/ <sup>235</sup> U	1σ		<sup>207</sup> Pb/ <sup>206</sup> Pb	1σ
Li08-24	17.86	671.06	298.76	0.0283	0.0002	0.1936	0.0021	0.0494	0.0006	0.0118	0.0001	0.2934	0.0008	179.90	2.46	179.70	3.50	165.81	55.63	99.89
Li08-25	11.26	362.79	348.50	0.0286	0.0002	0.1922	0.0062	0.0486	0.0014	0.0105	0.0001	0.7512	0.0064	181.78	2.46	178.50	10.35	127.52	132.87	98.20
Li16-01	3.23	101.85	118.05	0.0278	0.0003	0.2002	0.0114	0.0520	0.0029	0.0118	0.0005	0.4866	0.0043	176.76	3.69	185.30	18.90	284.38	249.99	95.17
Li16-02	6.43	186.97	86.33	0.0282	0.0003	0.2043	0.0071	0.0526	0.0017	0.0131	0.0007	0.4091	0.0129	179.27	3.69	188.76	11.73	310.56	144.19	94.71
Li16-03	5.67	133.21	72.32	0.0282	0.0004	0.1998	0.0224	0.0511	0.0042	0.0437	0.0017	0.3689	0.002	179.27	4.92	184.96	37.15	244.31	371.10	96.83
Li16-04	2.34	52.12	84.74	0.0284	0.0004	0.2081	0.0255	0.0520	0.0058	0.0232	0.0023	0.3117	0.0039	180.53	4.91	191.96	42.01	284.38	499.97	93.67
Li16-05	3.41	93.86	56.12	0.0287	0.0003	0.2021	0.0143	0.0511	0.0035	0.0126	0.0006	0.4872	0.0093	182.41	3.68	186.90	23.67	244.31	309.25	97.54
Li16-06	3.14	114.23	67.28	0.0281	0.0003	0.1978	0.0096	0.0512	0.0023	0.0102	0.0004	0.4667	0.0028	178.65	3.69	183.26	15.95	248.81	202.66	97.42
Li16-07	2.98	110.36	119.73	0.0274	0.0003	0.1936	0.0110	0.0510	0.0027	0.0105	0.0004	0.4043	0.0024	174.26	3.69	179.70	18.34	239.79	239.23	96.88
Li16-08	3.02	106.97	86.40	0.0286	0.0003	0.1886	0.0101	0.0478	0.0024	0.0113	0.0003	0.5823	0.0037	181.78	3.69	175.43	16.91	88.32	233.29	96.51
Li16-09	2.34	52.12	72.42	0.0284	0.0004	0.2081	0.0255	0.0520	0.0058	0.0232	0.0023	0.3117	0.0039	180.53	4.91	191.96	42.01	284.38	499.97	93.67
Li16-10	4.12	117.43	59.61	0.0285	0.0003	0.1898	0.0092	0.0482	0.0021	0.0124	0.0003	0.5769	0.001	181.15	3.69	176.46	15.39	108.03	201.69	97.41
Li16-11	2.81	89.23	169.27	0.0283	0.0003	0.2006	0.0113	0.0512	0.0026	0.0132	0.0007	0.3998	0.0015	179.90	3.69	185.63	18.73	248.81	229.09	96.81
Li16-12	3.98	154.08	67.64	0.0174	0.0003	0.1951	0.0116	0.0816	0.0045	0.0056	0.0002	1.3953	0.0119	111.20	3.73	180.97	19.32	1235.05	212.00	37.26
Li16-13	4.36	120.76	63.62	0.0287	0.0003	0.1917	0.0104	0.0482	0.0024	0.0142	0.0007	0.3707	0.0036	182.41	3.68	178.08	17.37	108.03	230.51	97.62
Li16-14	7.25	456.75	97.86	0.0275	0.0003	0.1986	0.0043	0.0525	0.0007	0.0144	0.0002	0.3992	0.0017	174.88	3.69	183.94	7.14	306.22	59.53	94.82
Li16-15	4.05	134.79	64.10	0.0274	0.0002	0.1932	0.0082	0.0508	0.0020	0.0097	0.0003	0.4419	0.0014	174.26	2.46	179.36	13.68	230.73	178.19	97.07
Li16-16	5.21	167.87	108.06	0.0279	0.0003	0.2113	0.0070	0.0546	0.0016	0.0112	0.0002	0.5971	0.0005	177.39	3.70	194.64	11.50	394.87	128.80	90.28
Li16-17	4.13	112.03	83.18	0.0284	0.0003	0.2012	0.0113	0.0515	0.0027	0.0136	0.0003	0.6304	0.0027	180.53	3.69	186.14	18.72	262.24	235.94	96.89
Li16-18	3.31	99.56	156.78	0.0268	0.0003	0.1968	0.0118	0.0530	0.0031	0.0087	0.0003	0.5419	0.0045	170.49	3.69	182.41	19.62	327.78	260.16	93.01
Li16-19	3.05	101.61	154.67	0.0278	0.0003	0.184	0.0111	0.0478	0.0027	0.0091	0.0004	0.4235	0.0004	176.76	3.69	171.50	18.66	88.32	262.45	97.02
Li16-20	3.35	110.14	197.52	0.0247	0.0003	0.2503	0.0093	0.0732	0.0024	0.0072	0.0002	0.7047	0.0045	157.29	3.70	226.82	14.80	1018.58	130.14	55.80
Li16-21	2.84	85.58	76.83	0.0286	0.0003	0.2073	0.0138	0.0526	0.0034	0.0115	0.0004	0.6288	0.0014	181.78	3.69	191.28	22.75	310.56	288.39	94.77
Li16-22	4.26	116.75	59.30	0.0277	0.0003	0.1901	0.0105	0.0496	0.0027	0.0074	0.0002	0.6737	0.0015	176.14	3.69	176.71	17.56	175.24	248.89	99.68
Li16-23	4.35	127.63	45.94	0.0238	0.0002	0.3121	0.0070	0.0948	0.0022	0.0076	0.0002	0.7812	0.002	151.63	2.47	275.81	10.62	1523.26	85.73	18.10
Li16-24	3.03	110.02	45.74	0.0272	0.0003	0.2021	0.0100	0.0530	0.0025	0.0076	0.0003	0.5595	0.0011	173.00	3.69	186.90	16.56	327.78	209.81	91.97
Li16-25	2.05	52.14	73.67	0.0274	0.0005	0.2019	0.0240	0.0532	0.0064	0.0079	0.0009	0.4422	0.0015	174.26	6.15	186.73	39.74	336.32	534.27	92.84
Li21-01	2.98	83.78	79.45	0.0279	0.0007	0.2008	0.0159	0.0521	0.0037	0.0104	0.0004	0.9261	0.0022	177.39	8.60	185.80	26.35	288.77	318.08	95.26
Li21-02	3.12	104.21	86.43	0.0286	0.0006	0.2115	0.0120	0.0535	0.0030	0.0112	0.0004	0.4937	0.0063	181.78	7.37	194.81	19.71	349.04	248.47	92.83
Li21-03	3.04	85.86	71.32	0.0281	0.0006	0.1993	0.0156	0.0512	0.0038	0.0092	0.0003	0.7481	0.0013	178.65	7.37	184.53	25.89	248.81	334.82	96.71
Li21-04	3.56	249.76	178.57	0.0285	0.0004	0.2088	0.0091	0.0531	0.0021	0.0173	0.0006	0.3916	0.0009	181.15	4.91	192.55	14.98	332.05	175.77	93.71
Li21-05	6.82	232.78	165.13	0.0285	0.0006	0.2161	0.0064	0.0548	0.0014	0.0098	0.0002	0.4832	0.0036	181.15	7.37	198.66	10.47	403.07	112.13	90.33
Li21-06	8.89	290.56	186.20	0.0281	0.0004	0.2108	0.0050	0.0542	0.0012	0.0086	0.0001	0.7028	0.0046	178.65	4.92	194.22	8.22	378.36	97.60	91.28
Li21-07	3.86	143.12	92.49	0.0276	0.0004	0.1964	0.0096	0.0514	0.0025	0.0085	0.0003	0.6155	0.0083	175.51	4.92	182.08	15.97	257.78	219.07	96.26
Li21-08	2.13	77.23	56.70	0.0272	0.0006	0.2117	0.0132	0.0562	0.0033	0.0086	0.0003	0.7927	0.0017	173.00	7.38	194.98	21.68	459.28	255.22	87.29
Li21-09	3.05	85.76	46.33	0.0274	0.0005	0.1985	0.0134	0.0527	0.0036	0.0084	0.0002	0.7716	0.0032	174.26	6.15	183.86	22.25	314.88	304.54	94.49
Li21-10	3.07	92.96	59.61	0.0272	0.0006	0.1947	0.0124	0.0520	0.0033	0.0087	0.0003	0.7753	0.0013	173.00	7.38	180.63	20.66	284.38	284.47	95.59
Li21-11	6.92	232.78	169.32	0.0281	0.0007	0.2094	0.0065	0.0538	0.0015	0.0098	0.0002	0.4677	0.0034	178.65	8.60	193.05	10.70	361.67	123.27	91.94
Li21-12	9.76	454.63	274.56	0.0285	0.0003	0.2156	0.0064	0.0546	0.0013	0.0153	0.0005	0.5416	0.0050	181.15	3.69	198.24	10.48	394.87	104.65	90.57
Li21-13	3.96	147.69	66.53	0.0275	0.0004	0.1902	0.0081	0.0501	0.0021	0.0086	0.0002	0.6532	0.0007	174.88	4.92	176.80	13.54	198.59	190.83	98.90
Li21-14	3.97	119.05	86.96	0.0286	0.0004	0.2091	0.0098	0.0528	0.0023	0.0143	0.0004	0.5704	0.0025	181.78	4.91	192.80	16.13	319.19	194.05	93.94
Li21-15	2.98	89.16	64.10	0.0278	0.0006	0.2084	0.0154	0.0543	0.0037	0.0129	0.0004	0.6981	0.0016	176.76	7.38	192.21	25.36	382.50	300.16	91.26
Li21-16	4.02	119.24	90.10	0.0271	0.0005	0.1928	0.0100	0.0515	0.0026	0.0112	0.0003	0.5174	0.0029	172.37	6.15	179.02	16.68	262.24	227.20	96.14
Li21-17	2.13	66.79	48.31	0.0274	0.0006	0.2147	0.0152	0.0568	0.0038	0.0087	0.0004	0.7117	0.0014	174.26	7.38	197.49	24.90	482.78	289.60	86.67
Li21-18	3.22	85.13	45.23	0.0273	0.0005	0.2081	0.0144	0.0551	0.0036	0.0094	0.0004	0.6653	0.0051	173.63	6.15	191.96	23.72	415.28	286.16	89.44
Li21-19	2.94	111.24	90.11	0.0272	0.0004	0.2067	0.0106	0.0548	0.0027	0.0096	0.0002	0.7742	0.0042	173.00	4.92	190.78	17.48	403.07	216.25	89.72
Li21-20	6.59	228.76	202.17	0.0279	0.0003	0.2096	0.0058	0.0542	0.0013	0.0091	0.0001	0.8583	0.0038	177.39	3.69	193.22	9.54	378.36	105.73	91.08
Li21-21	1.97	73.86	52.26	0.0274	0.0006	0.2092	0.0153	0.0551	0.0040	0.0097	0.0004	0.6371	0.0021	174.26	7.38	192.88	25.18	415.28	317.95	89.31
Li21-22	3.34	98.76	79.87	0.0276	0.0005	0.2044	0.0167	0.0537	0.0042	0.0112	0.0004	0.6293	0.0023	175.51	6.15	188.84	27.59	357.47	346.05	92.40

Table 1. Cont.

Spot No	Content (ppm)			Isotopic Ratios						Isotopic Ages (Ma)						Concordance (%)				
	Pb	U	Th	$\frac{^{206}\text{Pb}}{^{238}\text{U}}$	1 $\sigma$	$\frac{^{207}\text{Pb}}{^{235}\text{U}}$	1 $\sigma$	$\frac{^{207}\text{Pb}}{^{206}\text{Pb}}$	1 $\sigma$	$\frac{^{208}\text{Pb}}{^{232}\text{Th}}$	1 $\sigma$	$\frac{^{232}\text{Th}}{^{238}\text{U}}$	1 $\sigma$	$\frac{^{206}\text{Pb}}{^{238}\text{U}}$	1 $\sigma$		$\frac{^{207}\text{Pb}}{^{235}\text{U}}$	1 $\sigma$	$\frac{^{207}\text{Pb}}{^{206}\text{Pb}}$	1 $\sigma$
Li21-23	8.87	273.56	152.83	0.0281	0.0003	0.2193	0.0055	0.0564	0.0011	0.0163	0.0002	0.4736	0.0040	178.65	3.69	201.33	8.98	467.15	84.66	87.30
Li21-24	5.07	160.78	97.54	0.0279	0.0004	0.2165	0.0090	0.0561	0.0021	0.0135	0.0006	0.5213	0.0043	177.39	4.92	198.99	14.72	455.33	162.81	87.82
Li21-25	6.20	157.96	87.93	0.0275	0.0004	0.1991	0.0102	0.0522	0.0021	0.0241	0.0006	0.4734	0.0016	174.88	4.92	184.36	16.93	293.15	180.05	94.58



**Figure 4.** Zircon U-Pb Concordia diagram and weighted mean histogram of Late Jurassic granitoids from the Yangmugang area in the Lesser Xing’an–Zhangguangcai Range.

Sample LT16 was collected from the granodioritic porphyries located 5.6 km to the south of Yangmugang. The coordinates of the sampling point were  $45^{\circ}28'41''$  N,  $127^{\circ}40'40''$  E. The zircon grains exhibited transparent or semi-transparent euhedral to subhedral elongated prismatic crystals, with an elongated axis of 130–250  $\mu\text{m}$  and length/width ratios of 1.3:1–2.5:1. In the CL images, the zircon grains exhibited distinct magmatic oscillatory zoning (Figure 3), and the Th/U values of 25 measuring points ranged from 0.46 to 1.91 ( $>0.1$ ), indicating a typical magmatic origin for the zircons [36]. The age values for all the measurement points of sample LT16 were located on or near the Concordia curve (Figure 4c) and the weighted average age of 22 zircon grains was  $177.8 \pm 1.6$  Ma (MSWD = 0.9), representing the crystallization age. Additionally, three zircon grains had ages of  $111 \pm 4$  Ma,  $152 \pm 2$  Ma, and  $157 \pm 4$  Ma, which are the later magmatic hydrothermal event modification ages.

Sample LT21 was collected from the alkali feldspar granite located 11 km to the northwest of Yangmugang. The coordinates of the sampling point were  $45^{\circ}37'50''$  N,  $127^{\circ}37'15''$  E. The zircon grains were euhedral to subhedral elongated prismatic crystals, with an elongated axis of 150–200  $\mu\text{m}$  and length/width ratios of 1.5:1–2.0:1. In the CL images, the zircon grains exhibited distinct magmatic oscillatory zoning (Figure 3), and the Th/U values of 25 measuring points ranged from 0.29 to 1.68 ( $>0.1$ ), indicating a typical magmatic origin for the zircons [36]. The age values for all the measurement points of sample LT21 were located on or near the Concordia curve (Figure 4d). The weighted average age of the 25 zircon grains was  $177.2 \pm 2.2$  Ma (MSWD = 0.3), representing the crystallization age.

#### 4.2. Whole-Rock Major and Trace Elements

The major, trace, and rare earth element analysis results for the granodiorite, monzonitic granite, granite porphyry, and alkali feldspar granite samples are presented in Table 2.

**Table 2.** Major (wt.%) and trace (ppm) elements for Early Jurassic granotoids from Yangmugang area in the Lesser Xing’an-Zhangguangcai Range.

Sample	Granodiorite							Monzonitic Granite				
	Lt01	Lt02	Lt03	Lt04	Lt05	Lt06	Lt07	Lt08	Lt09	Lt10	Lt11	Lt12
SiO <sub>2</sub>	68.42	69.31	68.86	69.82	68.98	68.24	72.06	71.14	71.67	72.68	72.54	72.31
TiO <sub>2</sub>	0.43	0.4	0.34	0.32	0.31	0.39	0.27	0.22	0.26	0.28	0.29	0.2
Al <sub>2</sub> O <sub>3</sub>	14.99	14.73	15.16	15.09	15.04	15.59	13.71	14.66	14.69	13.78	13.37	13.45
TFe <sub>2</sub> O <sub>3</sub>	5.21	5.12	5.3	4.5	5.5	5.33	5.07	4.11	4.53	4.87	5.66	6.03
MnO	0.1	0.08	0.13	0.11	0.11	0.1	0.05	0.08	0.11	0.09	0.1	0.04
MgO	0.46	0.48	0.49	0.51	0.45	0.39	0.31	0.43	0.36	0.40	0.32	0.41
CaO	1.41	1.38	1.35	1.22	1.31	1.48	1.49	1.49	1.48	1.34	1.28	0.99
Na <sub>2</sub> O	4.43	4.39	4.34	4.42	4.54	4.57	4.04	3.86	4.08	3.58	4.01	3.96
K <sub>2</sub> O	4.17	4.19	4.09	3.97	3.86	3.75	4.07	4.38	3.72	3.94	3.56	3.69
P <sub>2</sub> O <sub>5</sub>	0.16	0.14	0.18	0.15	0.17	0.16	0.09	0.17	0.14	0.16	0.15	0.13
LOI	0.44	0.65	0.5	0.9	0.2	0.35	0.33	0.05	0.65	0.54	0.49	0.32
Total	99.52	99.96	99.96	99.89	99.99	99.75	100.86	100.32	100.80	100.89	100.97	100.89
Na <sub>2</sub> O + K <sub>2</sub> O	8.6	8.58	8.43	8.39	8.4	8.32	8.11	8.24	7.8	7.52	7.57	7.65
100 Mg/(Mg+Fe)	0.17	0.14	0.10	0.17	0.12	0.12	0.19	0.2	0.16	0.16	0.13	0.12
σ	2.91	2.80	2.75	2.62	2.72	2.74	2.26	2.41	2.12	1.91	1.94	2.00
A/CNK	1.04	1.03	1.08	1.09	1.07	1.09	1	1.06	1.09	1.09	1.05	1.09
A/NK	1.27	1.25	1.31	1.3	1.29	1.35	1.24	1.32	1.37	1.36	1.28	1.28
B	5.45	4.87	5.58	4.49	5.11	4.98	4.12	4.61	5.79	4.41	4.61	4.71
Li	17.6	16.7	25	23.6	20.7	21.7	27.5	30.9	20.1	34.2	28.3	28.2
V	39.09	35.89	48.21	42.04	41.31	42.05	16.81	48.2	56.65	56.8	58.19	47.33
Cr	20.45	15.66	19.84	16.99	18.24	17.5	18.8	21.5	21.5	20	15.86	19.53
Co	8.49	5.91	6.47	10.44	7.83	7.61	8.98	6.97	7.62	16.1	12.5	10.43
Ni	2.83	3.74	3.21	2.35	3.03	3.1	1.77	4.91	3.71	3.53	1.86	3.16
Sn	2.69	3.12	2.59	4.61	3.25	3.44	2.49	4.1	2.68	3.55	2.19	3
U	2.43	1.9	3.06	2.01	2.35	3.32	4.02	2.95	3.9	3.56	3.64	3.61
Rb	106	93	111	80	94	108	110	115	104	125	140	153
Ba	709	611	783	585	678	733	509	549	481	562	568	619
Th	15.15	10.41	17.97	13.81	14.73	16.7	14.31	15.74	13.65	15.81	16.51	16.94
U	2.43	1.89	3.32	2.01	2.35	3.06	4.51	4.64	4.59	4.89	4.95	5.02
Nb	12.46	10.76	14.27	11.52	11.86	13.29	10.88	13.8	12.56	14.25	14.49	14.71
Ta	1.42	1.17	1.74	1.26	1.35	1.47	0.97	1.41	1.07	1.43	1.5	1.57
Sr	352	296	310	287	301	316	264	239	258	248	218	262
Zr	156.01	131.98	143.10	122.45	136.89	150.1	160.42	143.12	150.95	147.17	134.95	159.11
Hf	6.12	4.78	5.53	4.24	5.34	5.57	7.61	6.54	7.05	6.57	6.42	7.17
Y	20.1	14.4	16.23	13.11	15.96	17.3	15.5	13.35	14.2	13.22	12.33	15.17
Ga	11.54	13.69	10.71	15.98	12.98	13.46	9.87	10.99	11.33	22.7	18.58	14.69
Cs	3.52	4.22	3.28	5.22	4.06	4.24	3.65	9.54	4.38	5.1	7.29	5.99
La	28.19	25.73	26.33	24.88	26.28	27.82	32.24	30.41	31.68	30.61	29.1	31.92
Ce	64.24	57.17	60.86	53.19	58.18	61.02	63.16	55.76	59.51	58.76	53.3	60.06
Pr	7.36	5.69	6.45	5.64	5.93	5.89	8.14	6.32	7.75	6.73	6.16	7.91
Nd	30.13	23.91	26.98	21.29	25.57	27.56	31.75	28.01	29.93	28.2	26.21	30.43
Sm	4.89	4.19	4.75	4.34	4.71	4.76	4.61	4.06	4.41	4.33	4.07	4.59
Eu	1.39	1.17	1.28	1.16	1.24	1.34	1.2	1.07	1.09	1.07	1.02	1.16
Gd	4.62	3.51	3.81	2.91	3.8	4.18	4.56	4.08	4.67	4.81	4.63	4.25
Tb	0.79	0.61	0.66	0.47	0.65	0.76	0.64	0.58	0.52	0.49	0.45	0.58
Dy	4.04	3.03	3.43	2.77	3.2	3.89	3.69	3.42	3.57	3.13	3.14	3.83
Ho	0.78	0.56	0.67	0.53	0.58	0.75	0.66	0.56	0.61	0.51	0.53	0.62
Er	2.45	1.89	1.97	1.85	1.94	2.04	2.48	2.29	2.4	2.02	2.21	2.42
Tm	0.42	0.34	0.38	0.3	0.35	0.41	0.46	0.42	0.44	0.39	0.41	0.45
Yb	2.76	2.22	2.43	2.19	2.34	2.53	2.91	2.77	2.81	2.59	2.73	2.83
Lu	0.39	0.29	0.33	0.28	0.32	0.35	0.42	0.39	0.4	0.37	0.34	0.41
δEu	0.88	0.91	0.89	0.94	0.87	0.9	0.79	0.8	0.73	0.71	0.72	0.79
δCe	1.05	1.09	1.09	1.04	1.08	1.09	0.92	0.92	0.89	0.95	0.91	0.89
(La/Yb) <sub>N</sub>	6.89	7.81	7.31	7.66	7.57	7.41	7.47	7.4	7.6	7.97	7.19	7.6
ΣREE	152.45	130.31	140.33	121.80	135.09	143.30	156.92	140.14	149.79	144.01	134.30	151.46
Sample	Monzonitic granite				Granite porphyry				Alkalic feldspar granite			
	Lt13	Lt14	Lt15	Lt16	Lt17	Lt18	Lt19	Lt20	Lt21	Lt22	Lt23	Lt24
SiO <sub>2</sub>	73.15	71.76	71.68	73.62	74.28	73.12	72.65	73.42	72.56	73.96	72.94	73.49
TiO <sub>2</sub>	0.21	0.25	0.3	0.14	0.11	0.16	0.1	0.09	0.07	0.07	0.11	0.1
Al <sub>2</sub> O <sub>3</sub>	13.39	13.92	14.45	13.16	12.24	13.36	13.48	13.78	13.56	12.94	13.95	13.27
TFe <sub>2</sub> O <sub>3</sub>	4.78	5.06	4.67	5.03	4.9	4.93	4.76	4.46	4.81	4.73	4.48	4.57
MnO	0.06	0.04	0.07	0.03	0.01	0.04	0.01	0.05	0.06	0.01	0.04	0.02
MgO	0.37	0.31	0.35	0.32	0.34	0.31	0.41	0.2	0.21	0.23	0.24	0.19
CaO	1.24	1.21	1.37	0.74	0.85	0.83	0.84	0.61	0.69	0.72	0.56	0.7
Na <sub>2</sub> O	3.65	3.87	3.72	3.81	3.76	3.9	4.19	4.17	4.27	3.81	4.19	3.98
K <sub>2</sub> O	4.16	4.06	4.49	4.1	3.94	4.47	4.07	4.09	3.66	3.86	3.91	3.87
P <sub>2</sub> O <sub>5</sub>	0.10	0.14	0.12	0.03	0.04	0.04	0.04	0.09	0.06	0.04	0.06	0.04
LOI	0.03	0.44	0.34	0.19	0.7	0.73	0.42	0.44	0.28	0.5	0.62	0.3
Total	100.84	100.35	100.96	100.68	100.21	100.94	100.33	100.72	99.69	100.12	100.25	100
Na <sub>2</sub> O + K <sub>2</sub> O	7.81	7.93	8.21	7.91	7.70	8.37	8.26	8.26	7.93	7.67	8.10	7.85
100 Mg/(Mg+Fe)	0.19	0.16	0.19	0.14	0.14	0.13	0.17	0.17	0.18	0.18	0.19	0.18
σ	2.02	2.19	2.35	2.04	1.9	2.33	2.3	2.24	2.13	1.9	2.19	2.02
A/CNK	1.05	1.07	1.07	1.09	1.02	1.05	1.05	1.11	1.11	1.10	1.15	1.1
A/NK	1.27	1.29	1.31	1.23	1.17	1.19	1.19	1.22	1.23	1.24	1.25	1.23
B	4.86	4.72	4.73	5.84	7.64	6.23	4.17	5.32	3.52	4.08	6.09	4.75
Li	28.4	28.3	28.2	3.7	5.9	3.7	8.9	5.7	7.3	10.4	6.4	7.5
V	54.96	53.49	49	5.52	6.15	10	6.47	25.65	17.11	15.3	14.52	18.15
Cr	19.72	18.37	19.41	12.64	14.11	14.90	11.92	7.54	5.5	3.46	4.22	5.18
Co	10.8	11.24	10.58	11.1	7.49	12.15	12.3	9.63	11.9	15.5	14	12.76

Table 2. Cont.

Sample	Granodiorite							Monzonitic Granite				
	Lt01	Lt02	Lt03	Lt04	Lt05	Lt06	Lt07	Lt08	Lt09	Lt10	Lt11	Lt12
Ni	3.50	2.84	3.16	2.16	1.9	1.68	2.17	1.89	1.68	3.32	2.78	2.42
Sn	3.13	2.77	2.99	2.36	2.17	2.16	1.69	2.75	2.37	1.83	2.23	2.3
U	3.51	3.59	3.6	3.26	2.5	1.83	4.84	1.78	1.87	2.01	2.97	2.16
Rb	111	106	113	136	116	118	113	202	164	152	210	154
Ba	535	505	641	542	505	426	406	740	650	543	749	570
Th	15.00	13.91	17.64	19.2	16.56	16.46	15.62	19.44	19.09	17.59	19.94	18.97
U	4.61	4.60	6.56	3.84	3.49	3.26	2.83	3.87	3.78	3.16	3.97	3.67
Nb	13.62	13.57	16.31	16.21	16.09	15	12.98	12.21	11.89	8.27	13.1	9.98
Ta	1.4	1.2	1.97	1.16	0.98	0.87	0.83	1.02	0.98	0.76	1.14	0.83
Sr	262.75	267.22	336.36	245.11	256.7	267.01	252.19	230	186.18	198.05	213.02	214.25
Zr	160.1	162.07	170.96	175.20	159.18	181.29	180.33	170.34	147.27	157.09	161.75	168.01
Hf	7.39	7.67	7.8	9.86	9.42	10.36	10.21	13.45	10.15	12.41	12.86	13.24
Y	16.1	17.5	19.11	14.9	12.9	16.7	20.8	14.50	9.2	9.45	10.36	12.71
Ga	15.9	16.39	15.06	10.57	19.51	9.2	17.44	14	23.6	16.5	19.3	18.35
Cs	6.58	6.62	6.14	3.57	3.14	3.84	3.10	0.8	1.93	2.62	1.12	1.62
La	32.13	33.56	35.59	30.41	24.88	32.19	28.8	36.41	27.8	30.49	31.22	32.23
Ce	60.64	65.38	65.61	60.34	59.61	63.49	61.71	54.43	39.31	40.46	41.69	45.97
Pr	8.01	8.37	8.54	7.06	6.59	8.73	7.67	5.72	4.55	4.71	5.03	5.32
Nd	30.96	32.52	34.77	25.22	24.01	28.23	28.19	23.89	16.44	21.21	21.33	22.72
Sm	4.61	5.41	6.37	4.37	4.09	5.01	4.71	3.48	2.75	2.87	3.33	3.38
Eu	1.19	1.26	1.32	1.07	0.99	1.20	1.18	0.76	0.64	0.65	0.67	0.72
Gd	4.65	4.32	4.85	4.09	3.33	4.23	4.11	3.27	2.79	2.87	2.94	3.17
Tb	0.61	0.71	0.75	0.56	0.46	0.78	0.68	0.51	0.36	0.39	0.40	0.43
Dy	3.88	3.97	4.55	2.84	2.24	3.83	3.65	2.69	1.94	2.01	2.22	2.24
Ho	0.63	0.71	0.75	0.55	0.44	0.72	0.76	0.55	0.31	0.38	0.39	0.45
Er	2.47	2.54	2.73	1.80	1.52	2.33	2.04	1.85	1.55	1.58	1.62	1.68
Tm	0.46	0.51	0.58	0.34	0.26	0.42	0.4	0.34	0.2	0.24	0.27	0.31
Yb	2.88	3.49	3.54	2.19	1.77	2.71	2.19	2.08	1.46	1.57	1.55	1.68
Lu	0.42	0.47	0.51	0.33	0.26	0.38	0.39	0.28	0.17	0.20	0.24	0.25
δEu	0.78	0.77	0.7	0.76	0.8	0.78	0.8	0.68	0.7	0.69	0.64	0.66
δCe	0.89	0.92	0.88	0.96	1.10	0.90	0.98	0.82	0.77	0.73	0.73	0.77
(La/Yb) <sub>N</sub>	7.52	6.48	6.78	9.36	9.48	8.01	8.87	11.80	12.84	13.09	13.58	12.93
ΣREE	153.54	163.22	170.46	141.17	130.45	154.25	146.48	136.26	100.27	109.63	112.90	120.55

4.2.1. Major Elements

The granodiorite samples had compositions of SiO<sub>2</sub> = 67.98%–69.82%, Al<sub>2</sub>O<sub>3</sub> = 14.16%–15.04%, K<sub>2</sub>O = 3.06%–3.79%, Na<sub>2</sub>O = 4.04%–4.37%, CaO = 0.95%–1.98%, MgO = 0.99%–1.54%, (Na<sub>2</sub>O + K<sub>2</sub>O) = 7.10%–8.00%, A/CNK = 1.00–1.11, and σ = 2.62–2.91. The rock samples were plotted into the granodiorite fields on a TAS diagram (Figure 5a), and it was determined that they belong to the high-K calc-alkaline series of weakly peraluminous rocks (Figure 5b,c).

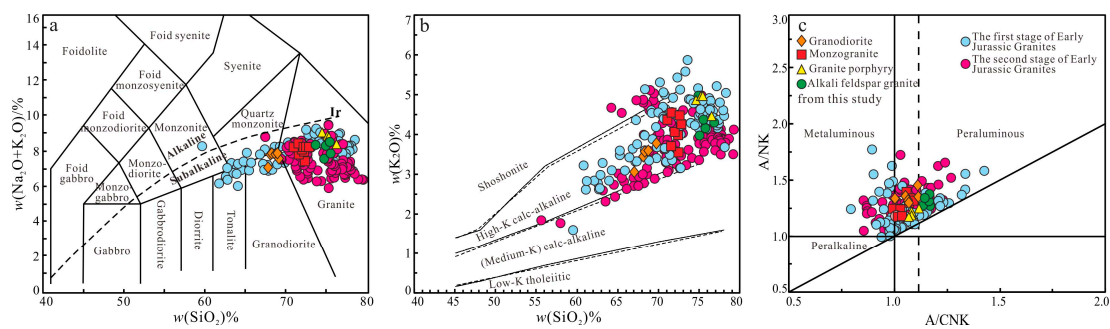


Figure 5. TAS diagram (a) (modified from [37]), SiO<sub>2</sub>-K<sub>2</sub>O diagram (b) (modified from [38]), and A/CNK-A/NK diagram (c) (modified from [39]) of Late Jurassic granitoids from the Yangmugang area in the Lesser Xing’an–Zhangguangcai Range (data collection was modified from [22–24,26,40–45]).

The monzonitic granite samples had compositions of SiO<sub>2</sub> = 71.14%–73.15%, Al<sub>2</sub>O<sub>3</sub> = 13.37%–14.93%, K<sub>2</sub>O = 3.56%–4.61%, Na<sub>2</sub>O = 3.56%–4.41%, CaO = 1.14%–1.84%, MgO = 0.84%–1.76%, (Na<sub>2</sub>O + K<sub>2</sub>O) = 7.55%–8.43%, A/CNK = 1.00–1.09, and σ = 1.98–2.41. The rock samples were plotted into the granite fields on a TAS diagram (Figure 5a), and it was determined that they belong to the high-K calc-alkaline series of weakly peraluminous rocks (Figure 5b,c).

The granite porphyry samples had compositions of  $\text{SiO}_2 = 74.65\%–76.62\%$ ,  $\text{Al}_2\text{O}_3 = 12.16\%–13.85\%$ ,  $\text{K}_2\text{O} = 4.46\%–4.97\%$ ,  $\text{Na}_2\text{O} = 3.86\%–4.19\%$ ,  $\text{CaO} = 0.54\%–0.84\%$ ,  $\text{MgO} = 0.21\%–0.51\%$ ,  $(\text{Na}_2\text{O} + \text{K}_2\text{O}) = 8.37\%–9.06\%$ ,  $\text{A/CNK} = 1.04–1.09$ , and  $\sigma = 1.89–2.30$ . The rock samples were plotted into the granite fields on a TAS diagram (Figure 5a), and it was determined that they belong to the high-K calc-alkaline series of weakly peraluminous–peraluminous rocks (Figure 5b,c).

The alkali feldspar granite samples had compositions of  $\text{SiO}_2 = 73.94\%–75.70\%$ ,  $\text{Al}_2\text{O}_3 = 13.07\%–13.88\%$ ,  $\text{K}_2\text{O} = 3.91\%–4.67\%$ ,  $\text{Na}_2\text{O} = 3.65\%–4.19\%$ ,  $\text{CaO} = 1.11\%–1.52\%$ ,  $\text{MgO} = 0.51\%–0.66\%$ ,  $(\text{Na}_2\text{O} + \text{K}_2\text{O}) = 7.56\%–8.56\%$ ,  $\text{A/CNK} = 1.06–1.15$ , and  $\sigma = 1.90–2.23$ . The rock samples were plotted into the granite fields on a TAS diagram (Figure 5a), and it was determined that they belong to the high-K calc-alkaline series of weakly peraluminous–peraluminous rocks (Figure 5b,c).

In terms of the major elemental composition, the granitoids in the Yangmu Gang area all belong to the high-potassium calc-alkaline series of rocks (Figure 5b). The granodiorite and monzonitic granite are weakly peraluminous rocks, while the granite porphyry and alkali feldspar granite fall into the weakly peraluminous–peraluminous rock category (Figure 5c). Additionally, the granite porphyry and alkali feldspar granite exhibited a higher silica content relative to the granodiorite and monzonitic granite, with lower levels of aluminum, calcium, and iron and lower  $\text{K}_2\text{O}/\text{Na}_2\text{O}$  and  $\text{TFeO}/\text{MgO}$  ratios.

#### 4.2.2. Trace Elements

In the chondrite-normalized rare earth element distribution diagram (Figure 6a), the granodiorite samples exhibited a right-skewed pattern characterized by light rare earth enrichment and heavy rare earth depletion ( $(\text{La}/\text{Sm})_N = 3.11–4.18$ ,  $(\text{La}/\text{Yb})_N = 6.89–8.02$ ,  $(\text{Gd}/\text{Yb})_N = 1.06–1.35$ ), with a subtle negative Eu anomaly ( $\delta\text{Eu} = 0.88–0.94$ ). In the primitive mantle-normalized trace element spider diagram (Figure 6b), these samples displayed the geochemical characteristics of enrichment in elements such as Rb, Th, U, K, Zr, and Hf, while they were relatively depleted in elements such as Ba, Sr, Nb, P, and Ti.

In the chondrite-normalized rare earth element distribution diagram (Figure 6a), the monzonitic granite samples exhibited a right-skewed pattern characterized by light rare earth enrichment and heavy rare earth depletion ( $(\text{La}/\text{Sm})_N = 4.15–5.20$ ,  $(\text{La}/\text{Yb})_N = 8.39–10.18$ ,  $(\text{Gd}/\text{Yb})_N = 1.0–1.34$ ), with a subtle negative Eu anomaly ( $\delta\text{Eu} = 0.81–0.95$ ). In the primitive mantle-normalized trace element spider diagram (Figure 6b), these samples displayed the geochemical characteristics of enrichment in elements such as Rb, Th, U, K, Zr, and Hf, while they were relatively depleted in elements such as Ba, Sr, Nb, P, and Ti.

In the chondrite-normalized rare earth element distribution diagram (Figure 6c), the granite porphyry samples exhibited a right-skewed pattern characterized by light rare earth enrichment and heavy rare earth depletion ( $(\text{La}/\text{Sm})_N = 4.04–5.38$ ,  $(\text{La}/\text{Yb})_N = 8.01–9.48$ ,  $(\text{Gd}/\text{Yb})_N = 1.22–1.91$ ), with a moderate negative Eu anomaly ( $\delta\text{Eu} = 0.70–0.80$ ). In the primitive mantle-normalized trace element spider diagram (Figure 6d), these samples displayed the geochemical characteristics of enrichment in elements such as Rb, Th, U, K, Zr, and Hf, while they were relatively depleted in elements such as Ba, Sr, Nb, P, and Ti.

In the chondrite-normalized rare earth element distribution diagram (Figure 6c), the alkali feldspar granite samples exhibited a right-skewed pattern characterized by light rare earth enrichment and heavy rare earth depletion ( $(\text{La}/\text{Sm})_N = 5.83–7.39$ ,  $(\text{La}/\text{Yb})_N = 9.66–10.60$ ,  $(\text{Gd}/\text{Yb})_N = 1.02–1.25$ ), with a moderate negative Eu anomaly ( $\delta\text{Eu} = 0.67–0.70$ ). In the primitive mantle-normalized trace element spider diagram (Figure 6d), these samples displayed the geochemical characteristics of enrichment in elements such as Rb, Th, U, K, Zr, and Hf, while they were relatively depleted in elements such as Ba, Sr, Nb, P, and Ti.

In terms of the rare earth elemental composition, the granodiorite and monzonitic granite exhibited a weak negative Eu anomaly, while the granite porphyry and alkali feldspar granite showed a moderate negative Eu anomaly. Regarding the trace elemental composition, the granite porphyry and alkali feldspar granite showed greater depletion in their Sr, Nb, P, and Ti contents.

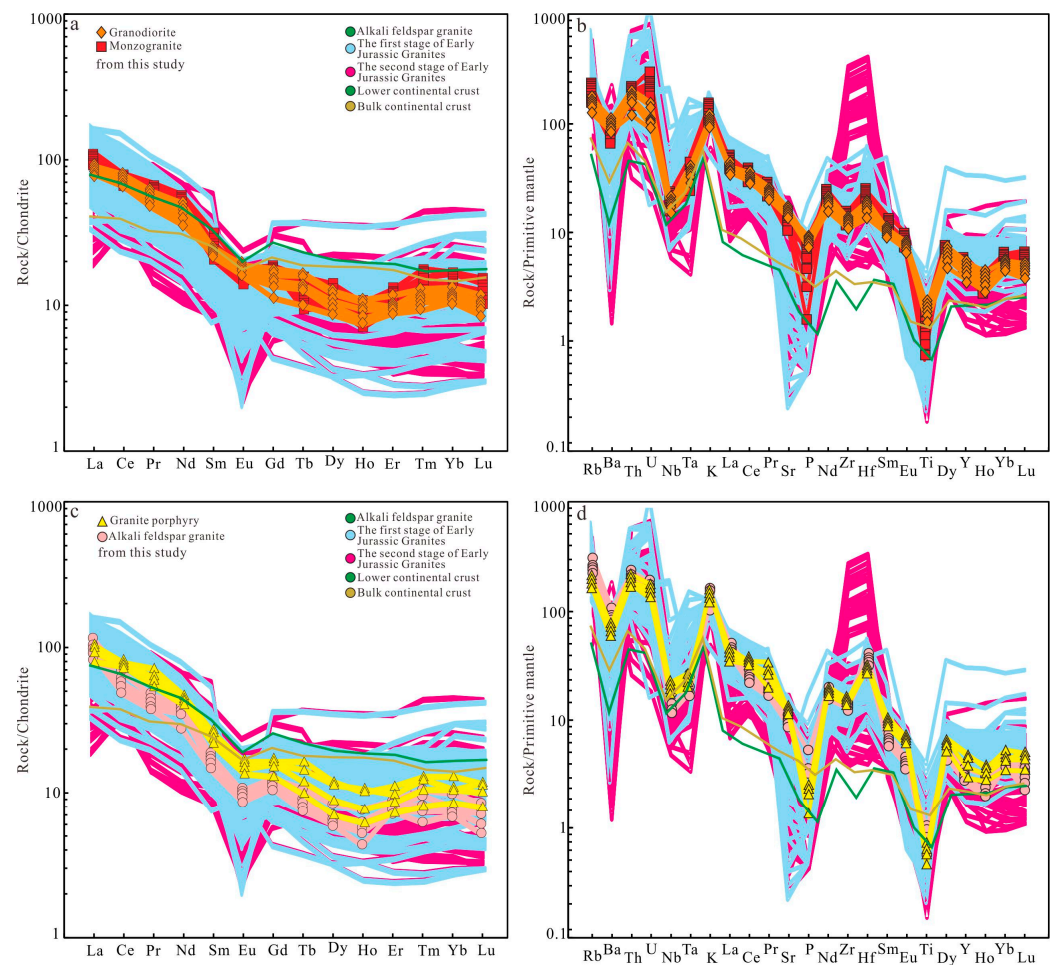


**Figure 6.** Chondrite-normalized REE distribution patterns (a,c) and primitive mantle-normalized multi-element spider diagrams (b,d) of Late Jurassic granitoids from the Yangmugang area in the Lesser Xing’an–Zhangguangcai Range (normalizing values modified from [46]).

## 5. Discussion

### 5.1. Spatial and Temporal Distribution of Early to Middle Mesozoic Granitoids from the LXZR

This study conducted U-Pb isotopic dating of granitoids in the Yangmugang area of the Lesser Xing’an–Zhangguangcai Range. The dating data points were situated near the Concordia curve in the U-Pb diagram (Figure 4). The zircon Th/U values were 0.21–1.91, all of which were greater than 0.1, indicating typical magmatic-origin zircons [36]. The dating results revealed that the weighted average ages of granodiorite, monzonitic granite, granite porphyry, and alkali feldspar granite in the Yangmugang area are  $182.9 \pm 1.4$  Ma,  $180.8 \pm 0.9$  Ma,  $177.8 \pm 1.6$  Ma and  $177.2 \pm 2.2$  Ma. The formation ages for all of them correspond to the Early Jurassic period.

Based on the zircon U-Pb geochronological data obtained from the Early Jurassic granitoids in the Yangmugang area and in combination with previous studies on Early to Middle Mesozoic zircon U-Pb dating results in the Lesser Xing’an–Zhangguangcai Range (Table 3), this study divided the Early to Middle Mesozoic magmatic activity in the Lesser Xing’an–Zhangguangcai Range into three distinct episodes (Figure 7a): (1) In the Late Triassic period (220–205 Ma), magmatic rocks were predominantly distributed at the southernmost tip of the Zhangguangcai Range, between  $129^\circ$  E and  $131^\circ$  E. The peak period of magmatic activity was around 216 Ma. The intrusive rock assemblage mainly comprises monzonitic granite, granodiorite, monzogranite, and alkali feldspar granite, with minor amounts of gabbro and monzonitic granite [30,47]. The volcanic rocks consist mainly of andesite–rhyolite assemblages, with the representative stratigraphic unit

being the Hongguang Formation in the Zhangguangcai Range [12,14]. (2) In the Early Jurassic phase I (198–182 Ma), the magmatic rocks were primarily distributed between 128° E and 130° E. The peak period of magmatic activity was around 186 Ma. These rocks exhibit a northeast–southwest-trending belt-like distribution [42]. The composition of the intermediate-acidic intrusive rock assemblage is dominated by granodiorite, diorite, and alkali feldspar granite [29]. They are characterized as high-K calc-alkaline rocks with weakly peraluminous to peraluminous characteristics. Basic intrusive rocks are found in areas such as Tielixi (187 Ma), Shuguang (186 Ma), Liuzhonggou (186 Ma), and Xincun (185 Ma) [14,22,23], and they exhibit a medium- to high-K calc-alkaline affinity with weakly peraluminous characteristics. The volcanic rocks constitute a sequence of basalt–basaltic andesite–rhyolite assemblages, with the representative rock being Hatoushan Formation rhyolite (184 Ma). These are high-K calc-alkaline rocks [14,20,48–79]. (3) In the Early Jurassic phase II (182–172 Ma), magmatic rocks were primarily distributed between 126° E and 128° E. The peak period of magmatic activity was around 178 Ma. The intermediate-acidic intrusive rock assemblage is dominated by granodiorite, monzogranite, and alkali feldspar granite [26,27]. A smaller number of volcanic rocks are distributed, with the representative rock being Erlanghe Formation rhyolite (179.7 Ma), which belongs to the calc-alkaline series of rocks [23,24]. By summarizing the spatiotemporal distribution patterns of Early to Middle Mesozoic magmatic rocks in the Lesser Xing’an–Zhangguangcai Range, this study revealed a trend of progressively younger magmatic activity from east to west in the area during the Early to Middle Mesozoic (Figure 7b–f). The Early Jurassic granitoids sampled from the Yangmugang area in this study constitute a significant component of the Late Jurassic tectonics and magmatic activity in the Lesser Xing’an–Zhangguangcai Range. Accurately determining the formation age of these granitic rocks holds crucial significance for understanding the Early to Middle Mesozoic tectonic–magmatic evolution processes in the Lesser Xing’an–Zhangguangcai Range.

**Table 3.** Geochronological data for the Early Mesozoic Era intrusive rocks in the Lesser Xing’an–Zhangguangcai Range.

Order	Sample	Latitude	Longitude	Location	Lithology	Age (Ma)	Method	Reference
1	Lt02	45°34′05″	127°34′25″	Yangmugang	Granodiorite	182.9 ± 1.4	LA-ICP-MS	This paper
2	Lt08	45°29′03″	127°32′45″	Yangmugang	Monzonitic granite	180.8 ± 0.9	LA-ICP-MS	This paper
3	Lt16	45°28′41″	127°40′40″	Yangmugang	Granite porphyry	177.8 ± 1.6	LA-ICP-MS	This paper
4	Lt21	45°37′50″	127°37′15″	Yangmugang	Alkalic feldspar granite	177.2 ± 2.2	LA-ICP-MS	This paper
5	9718-1	43°50′54″	126°58′50″	Tianqiaogang	Alkali feldspar granite	190.0 ± 2.0	TIMS	[2]
6	9757-4	46°03′45″	128°59′55″	Maojiatun	Alkali feldspar granite	212.0 ± 2.0	TIMS	[2]
7	9767-2	46°31′05″	128°49′51″	Milin	Syenogranite	197.0 ± 2.0	TIMS	[2]
8	H15-08	46°55′05″	128°11′06″	Taoshanzhen	Diorite	181.0 ± 1.0	LA-ICP-MS	[14]
9	H15-11	46°55′29″	128°20′42″	Shenshuzhen	Granodiorite	178.0 ± 2.0	LA-ICP-MS	[14]
10	H15-14	46°57′51″	128°42′17″	Shenshuzhen	Monzogranite	191.0 ± 1.0	LA-ICP-MS	[14]
11	H15-16	47°02′49″	129°06′19″	Langxiangzhen	Monzogranite	195.0 ± 2.0	LA-ICP-MS	[14]
12	H15-34	47°23′09″	129°29′33″	Tiexijie	Syenogranite	210.0 ± 1.0	LA-ICP-MS	[14]
13	H15-35	47°23′30″	129°37′30″	Tiexijie	Monzogranite	220.0 ± 1.0	LA-ICP-MS	[14]
14	H15-37	47°24′31″	129°47′34″	Wujiazi	Granodiorite	251.0 ± 1.0	LA-ICP-MS	[14]
15	H15-38	47°23′58″	129°54′25″	Wujiazi	Syenogranite	242.0 ± 2.0	LA-ICP-MS	[14]
16	H15-39	47°23′00″	129°58′57″	Dalazi	Diorite	246.0 ± 1.0	LA-ICP-MS	[14]
17	H15-40	47°23′00″	129°58′57″	Dalazi	Monzogranite	241.0 ± 1.0	LA-ICP-MS	[14]
18	H15-61-5	45°23′27″	127°13′42″	Yuquan	Monzodiorite	179.0 ± 3.0	LA-ICP-MS	[15]
19	H15-63-1	45°17′03″	127°29′59″	Mao’ershan	Monzogranite	181.0 ± 1.0	LA-ICP-MS	[15]
20	H15-66-1	45°23′19″	127°41′12″	Jidiantun	Monzogranite	180.0 ± 1.0	LA-ICP-MS	[15]
21	H15-68-1	45°19′27″	127°50′31″	Yiman village	Granodiorite	174.0 ± 1.0	LA-ICP-MS	[15]
22	H15-69-1	45°07′58″	128°25′21″	Shangzhi	Granodiorite	189.0 ± 1.0	LA-ICP-MS	[15]



Table 3. Cont.

Order	Sample	Latitude	Longitude	Location	Lithology	Age (Ma)	Method	Reference
23	H15-70-1	45°07'58"	128°25'22"	Shangzhi	Syenogranite	200.0 ± 1.0	LA-ICP-MS	[15]
24	H15-71-1	45°04'35"	128°30'00"	Shangzhi	Monzogranite	198.0 ± 2.0	LA-ICP-MS	[15]
25	H15-72-1	44°51'35"	128°41'39"	Shangzhi	Monzogranite	193.0 ± 1.0	LA-ICP-MS	[15]
26	X-4			Xinhuatun	Granodiorite	184.0 ± 4.0	SHRIMP	[18]
27	HTW1-1	48°32'24"	129°12'51"	Xincun	Hornblende-gabbro	185.0 ± 1.0	LA-ICP-MS	[22]
28	HTW6-1	48°29'35"	129°25'21"	Shuguang	Olivine-gabbro	186.0 ± 2.0	LA-ICP-MS	[22]
29	HYC10-1	47°42'37"	128°23'23"	Xinhuo	Hornblende-gabbro	182.0 ± 2.0	LA-ICP-MS	[22]
30	HWC1-1	45°08'29"	127°14'02"	Pingfang	Gabbro-diorite	183.0 ± 1.0	LA-ICP-MS	[22]
31	HYL1-1	46°20'54"	128°01'09"	Liuzhonggou	Hornblendite	186.0 ± 2.0	LA-ICP-MS	[22]
32	06TM-2	43°02'31"	129°40'28"	Tumen	Gabbro	187.0 ± 1.0	SHRIMP	[23]
33	HSW2-6	48°42'51"	127°15'43"	Xinfu forest farm	Monzogranite	176.0 ± 1.0	LA-ICP-MS	[23]
34	HSW23	49°43'07"	127°20'23"	Fengshuigou	Monzogranite	175.0 ± 1.0	LA-ICP-MS	[23]
35	HSWG-2	48°41'55"	127°25'15"	Xinfu forest farm	Sycamore granite	185.0 ± 2.0	LA-ICP-MS	[23]
36	HSW6-4	48°41'55"	127°25'15"	Xinfu forest farm	Sycamore granite	183.0 ± 2.0	LA-ICP-MS	[23]
37	9766-1	46°55'42"	128°53'15"	Langxiang	Granodiorite	200.0 ± 2.0	LA-ICP-MS	[25]
38	9773-1	46°43'00"	128°47'14"	Tuanjie	Monzogranite	201.0 ± 3.0	LA-ICP-MS	[25]
39	9777-1	46°56'17"	128°17'51"	Shichang	Granodiorite	175.0 ± 2.0	LA-ICP-MS	[25]
40	P40-1	47°35'28"	129°14'23"	Taiqing	Monzonite	210.0 ± 2.0	LA-ICP-MS	[25]
41	97SW001	45°12'14"	127°48'13"	Wujimi	Syenogranite	180.0 ± 3.0	SHRIMP	[25]
42	97SW005	45°05'05"	128°07'32"	Yimianpo	Granodiorite	183.0 ± 4.0	SHRIMP	[25]
43	97SW008	44°55'49"	128°54'38"	Yimianpo	Felsic dyke	147.0 ± 10	SHRIMP	[25]
44	97SW009	44°55'49"	128°54'38"	Hufeng	Monzogranite	179.0 ± 7.0	SHRIMP	[25]
45	98SW101	45°47'26"	128°30'13"	Yanshou	Syenogranite	199.0 ± 5.0	SHRIMP	[25]
46	98SW103	45°47'51"	128°30'21"	Yanshou	Granodiorite	191.0 ± 4.0	SHRIMP	[25]
47	98SW104	45°47'51"	128°30'21"	Yanshou	Felsic dyke	147.0 ± 6.0	SHRIMP	[25]
48	97SW009	44°55'49"	128°54'38"	Hufeng	Monzogranite	179.0 ± 7.0	SHRIMP	[25]
49	98SW101	45°47'26"	128°30'13"	Yanshou	Syenogranite	199.0 ± 5.0	SHRIMP	[25]
50	98SW103	45°47'51"	128°30'21"	Yanshou	Granodiorite	191.0 ± 4.0	SHRIMP	[25]
51	98SW104	45°47'51"	128°30'21"	Yanshou	Felsic dyke	147.0 ± 6.0	SHRIMP	[25]
52	98SW122	43°34'31"	127°34'22"	Baishishan	Granodiorite	190.0 ± 2.0	SHRIMP	[25]
53	98SW124	43°58'10"	126°43'44"	Jiangmifeng	Granodiorite	173.0 ± 4.0	SHRIMP	[25]
54	98SW125	43°53'56"	126°55'01"	Tiangan	Monzogranite	175.0 ± 3.0	SHRIMP	[25]
55	98SW126	43°53'56"	126°55'01"	Tiangan	Dioritic enclave	175.0 ± 4.0	SHRIMP	[25]
56	00SW225	47°41'50"	128°58'00"	Hongqi	Granodiorite	198.0 ± 4.0	SHRIMP	[25]
57	00SW231	47°24'15"	129°24'36"	Dafeng	Monzogranite	201.0 ± 4.0	SHRIMP	[25]
58	DY0380-1	47°27'22"	129°14'40"	Xiaoxilin	Granodiorite	200.0 ± 3.0	LA-ICP-MS	[25]
59	DY0385-1	47°38'48"	129°02'55"	Chaoxiantun	Alkali feldspar granite	176.0 ± 2.0	LA-ICP-MS	[25]
60	DY0535-1	44°30'15"	129°15'19"	Shihecun	Syenogranite	192.0 ± 1.0	LA-ICP-MS	[25]
61	DY0540-1	44°31'33"	128°48'19"	Fahecun	Syenogranite	196.0 ± 1.0	LA-ICP-MS	[25]
62	DY0545-1	44°23'25"	129°03'38"	Jiujiecun	Syenogranite	185.0 ± 2.0	LA-ICP-MS	[25]
63	DY0556-1	45°23'03"	127°41'45"	Jijiadian	Syenogranite	190.0 ± 1.0	LA-ICP-MS	[25]
64	DY103-2	44°26'01"	126°46'30"	Liangjishan	Alkali feldspar granite	191.0 ± 2.0	LA-ICP-MS	[25]
65	DY104-2	44°20'18"	126°53'13"	Shulan	Granodiorite	190.0 ± 2.0	LA-ICP-MS	[25]
66	DY105-2	44°14'27"	126°54'28"	Xiangshui	Monzogranite	172.0 ± 3.0	LA-ICP-MS	[25]
67	DY118-1	43°05'06"	126°45'03"	Baishishan	Granodiorite	182.0 ± 2.0	LA-ICP-MS	[25]
68	DY144-1	43°51'16"	126°31'31"	Beishan	Syenogranite	166.0 ± 2.0	LA-ICP-MS	[25]
69	FW02-184	43°34'22"	127°34'30"	Baishishan	Granodiorite	181.0 ± 2.0	LA-ICP-MS	[25]
70	FW02-188	43°38'49"	127°44'52"	Baishishan	Granodiorite	187.0 ± 4.0	LA-ICP-MS	[25]
71	9780-2	48°16'28"	129°47'03"	Qingshui	Alkali feldspar granite	222.0 ± 5.0	LA-ICP-MS	[25]
72	H15-10-01	46°55'05"	128°11'06"	Tieli	Syenogranite	190.0 ± 2.0	LA-ICP-MS	[26]
73	H15-55-01	46°12'06"	128°39'11"	Tieli	Syenogranite	196.0 ± 1.0	LA-ICP-MS	[26]
74	H15-56-01	46°16'02"	128°32'08"	Tieli	Syenogranite	196.0 ± 1.0	LA-ICP-MS	[26]
75	H15-57-01	46°25'23"	128°31'32"	Tieli	Tonalite	186.0 ± 1.0	LA-ICP-MS	[26]
76	H15-58-01	46°26'30"	128°32'15"	Tieli	Granodiorite	181.0 ± 1.0	LA-ICP-MS	[26]
77	H15-59-01	46°33'42"	128°40'37"	Tieli	Monzogranite	182.0 ± 1.0	LA-ICP-MS	[26]
78	H15-09-1	46°55'05"	128°11'06"	Taoshanzhen	Monzogranite	188.0 ± 1.0	LA-ICP-MS	[27]
79	LM-0101	47°22'08"	128°31'54"	Luming	Monzogranite	181.0 ± 2.0	LA-ICP-MS	[27]
80	LMN			Luming	Monzogranite	176.0 ± 2.0	LA-ICP-MS	[27]
81	CLN			Cuilin	Quartz monzonite	178.0 ± 1.0	LA-ICP-MS	[27]
82	HJHN1	48°31'33"	128°57'09"	Huojihe	Monzonitic granite	186.0 ± 1.7	LA-ICP-MS	[27]
83	DBZG-1	43°05'	126°30'	Huadian	Porphyritic dolerite	187.6 ± 1.5	LA-ICP-MS	[29]

Table 3. Cont.

Order	Sample	Latitude	Longitude	Location	Lithology	Age (Ma)	Method	Reference
84	MG-7	43°50'54"	126°58'50"	Tianqiaogang	Alkali feldspar granite	182.0 ± 3.0	SHRIMP	[40]
85	9718-1	43°50'15"	127°10'05"	Tiaoqiaogang	Alkali feldspar granite	188.0 ± 1.0	TIMS	[40]
86	9728-1			Sandaohu	Sycamore granite	216.0 ± 3.0	LA-ICP-MS	[40]
87	RT-09			Errenban	Monzonitic granite	176.4 ± 1.1	LA-ICP-MS	[42]
88	RT-11			Errenban	Monzonitic granite	178.3 ± 1.3	LA-ICP-MS	[42]
89	RT-14			Lonngtoushan	Monzonitic granite	177.7 ± 1.1	LA-ICP-MS	[42]
90	RT-04			Shenxiandong	Monzonitic granite	180.0 ± 1.8	LA-ICP-MS	[42]
91	RT-13			Maoershan	Monzonitic granite	179.9 ± 1.2	LA-ICP-MS	[42]
92	CC-1a	43°28'12"	125°05'12"	Kaoshan	Syenogranites	193.2 ± 1.0	LA-ICP-MS	[43]
93	CC-2a	43°23'32"	125°00'32"	Kaoshan	Syenogranites	190.3 ± 1.0	LA-ICP-MS	[44]
94	RT-07			Jiudingshan	Monzonitic granite	172.1 ± 1.3	LA-ICP-MS	[45]
95	RT-02			Jiudingshan	Monzonitic granite	172.1 ± 1.2	LA-ICP-MS	[45]
96	RT-03			Jiudingshan	Monzonitic granite	172.4 ± 1.2	LA-ICP-MS	[45]
97	RT-12			Jiudingshan	Monzonitic granite	172.2 ± 1.7	LA-ICP-MS	[45]
98	J005	43°59'10"	127°25'31"	Falazhen	Potassium feldspar granite	190.8 ± 2.3	LA-ICP-MS	[45]
99	015	44°04'26"	127°06'26"	Laoyelin	Potassium feldspar granite	185.2 ± 2.4	LA-ICP-MS	[45]
100	009	44°11'39"	127°22'28"	Shangyincun	Potassium feldspar granite	178.9 ± 2.7	LA-ICP-MS	[45]
101	014	44°15'21"	127°24'29"	Maoshan	Potassium feldspar granite	182.3 ± 3.0	LA-ICP-MS	[45]
102	013	44°15'21"	127°24'29"	Maoshan	Potassium feldspar granite	183.7 ± 2.4	LA-ICP-MS	[45]
103	RT-05	44°15'21"	127°24'29"	Maoshan	Monzonitic granite	178.9 ± 1.3	LA-ICP-MS	[45]
104	1160-1	44°47'15"	129°03'28"	Hengdaohezi	Syenite granite	198.5 ± 1.6	LA-ICP-MS	[47]
105	14HYC12-1	47°23'11"	129°58'06"	Hegang	Syenogranite	251.0 ± 2.0	LA-ICP-MS	[63]
106	16XH6-1	44°54'33"	129°20'52"	Hengdaohezi	Monzogranite	251.0 ± 2.0	LA-ICP-MS	[63]
107	14HYC17-1	47°12'15"	130°00'40"	Hegang	Monzogranite	249.0 ± 2.0	LA-ICP-MS	[63]
108	14HYC13-1	47°22'04"	130°02'18"	Hegang	Monzogranite	245.0 ± 2.0	LA-ICP-MS	[63]
109	15XH6-1	45°49'12"	129°28'10"	Shuguanglinchang	Monzogranite	215.0 ± 2.0	LA-ICP-MS	[63]
110	15XH11-1	45°42'40"	129°25'18"	Shuguanglinchang	Hornblende gabbro	215.0 ± 3.0	LA-ICP-MS	[63]
111	15XH4-1	45°41'59"	129°16'41"	Shuguanglinchang	Syenogranite	214.0 ± 2.0	LA-ICP-MS	[63]
112	18XH16-1	44°54'20"	129°31'24"	Hengdaohezi	Monzogranite	213.0 ± 1.0	LA-ICP-MS	[63]
113	15XH7-1	45°49'15"	129°28'08"	Shuguanglinchang	Gabbro	211.0 ± 2.0	LA-ICP-MS	[63]
114	15XH7-5	45°49'15"	129°28'08"	Shuguanglinchang	Gabbro	210.0 ± 2.0	LA-ICP-MS	[63]
115	15XH5-1	45°48'08"	129°20'09"	Shuguanglinchang	Monzogranite	204.0 ± 3.0	LA-ICP-MS	[63]
116	18H25-1	47°24'16"	129°24'37"	Hegang	Monzogranite	202.0 ± 2.0	LA-ICP-MS	[63]
117	15XH17-1	44°48'48"	129°06'21"	Hengdaohezi	Syenogranite	200.0 ± 2.0	LA-ICP-MS	[63]
118	18XH3-1	45° 01'33"	128°11'12"	Weihe	Quartz monzonite	196.0 ± 2.0	LA-ICP-MS	[63]
119	14HYC8-1	46°57'53"	129°16'50"	Chenming	Granodiorite	194.0 ± 1.0	LA-ICP-MS	[63]
120	18XH11-1	44°56'07"	128°32'52"	Weihe	Monzogranite	192.0 ± 1.0	LA-ICP-MS	[63]
121	18H1-1	46°55'06"	128°11'02"	Tieli	Monzogranite	190.0 ± 2.0	LA-ICP-MS	[63]
122	18XH12-1	44°51'24"	128°41'50"	Weihe	Quartz monzonite	189.0 ± 1.0	LA-ICP-MS	[63]
123	18XH10-1	44°50'26"	128°32'06"	Weihe	Quartz monzonite	187.0 ± 1.0	LA-ICP-MS	[63]
124	18XH2-1	45°23'19"	127°41'11"	Shangzhi	Monzogranite	181.0 ± 1.0	LA-ICP-MS	[63]
125	18XH1-1	45°12'44"	127°49'34"	Shangzhi	Syenogranite	177.0 ± 2.0	LA-ICP-MS	[63]
126	14YB50-2	42°40'45"	130°27'22"	Yanbian	Diorite	198.0 ± 3.0	LA-ICP-MS	[80]
127	14YB42	42°35'07"	130°27'21"	Yanbian	Quartz diorite	197.0 ± 5.0	LA-ICP-MS	[80]
128	14YB33-6	42°41'54"	130°17'27"	Yanbian	Tonalite	197.0 ± 4.0	LA-ICP-MS	[80]
129	14YB41-1	42°33'28"	130°25'53"	Yanbian	Granodiorite	189.0 ± 3.0	LA-ICP-MS	[80]
130	14YB59	42°34'10"	130°31'47"	Yanbian	Syenogranite	199.0 ± 4.0	LA-ICP-MS	[80]
131	14YB62	42°31'10"	130°33'05"	Yanbian	Granodiorite	197.0 ± 3.0	LA-ICP-MS	[81]
132	16GW114	44°40'29"	129°34'23"	Fengshou village	Granodiorite	215.0 ± 1.0	LA-ICP-MS	[82]
133	16GW121	44°39'28"	129°22'53"	Xinmin village	Monzogranite	217.0 ± 1.0	LA-ICP-MS	[82]
134	16GW126	44°38'27"	129°22'40"	Hailin forest farm	Granodiorite	219.0 ± 1.0	LA-ICP-MS	[82]
135	16GW110	44°40'29"	129°34'23"	Fengshou village	Diorite	221.0 ± 1.0	LA-ICP-MS	[82]
136	16GW124	44°38'27"	129°22'40"	Hailin forest farm	Diorite	221.0 ± 1.0	LA-ICP-MS	[82]
137	LM1			Luming	Monzogranite	183.0 ± 2.0	LA-ICP-MS	[83]
138	LM1			Luming	Monzogranite	187.0 ± 2.0	LA-ICP-MS	[84]

Table 3. Cont.

Order	Sample	Latitude	Longitude	Location	Lithology	Age (Ma)	Method	Reference
139	LQ	42°43'07"	124°15'50"	Jiaohe	Granodiorite	160.0 ± 1.0	LA-ICP-MS	[85]
140	GZ	43°19'53"	127°25'49"	Jiaohe	Monzogranite	185.0 ± 1.0	LA-ICP-MS	[86]
141	ZQ	43°46'21"	126°39'07"	Jiaohe	Monzogranite	179.0 ± 1.0	LA-ICP-MS	[86]
142	YT	43°42'35"	126°39'02"	Jiaohe	Monzogranite	179.0 ± 1.0	LA-ICP-MS	[86]
143	DHS	43°31'59"	126°17'26"	Jiaohe	Andesite	177.0 ± 3.0	LA-ICP-MS	[86]
144	DB-91			Xunke County	Alkali feldspar granite	174.5 ± 0.7	LA-ICP-MS	[87]
145	DB-91			Xunke County	Alkali feldspar granite	173.0 ± 0.6	LA-ICP-MS	[87]
146	1087-4	44°57'26"	128°23'52"	Shangweihe	Biotite quartz diorite	197.0 ± 1.0	LA-ICP-MS	[88]
147	1089-2	44°57'01"	128°24'33"	Shangweihe	Quartz diorite	190.0 ± 1.0	LA-ICP-MS	[88]
148	1090-3	44°57'21"	128°25'24"	Shangweihe	Granodiorite	191.0 ± 1.0	LA-ICP-MS	[88]
149	1115-1	44°50'15"	128°41'40"	Shidaohezi	Granodiorite	195.0 ± 1.0	LA-ICP-MS	[88]
150	1126-1	45°01'31"	128°11'06"	Jiujiangpao	Granodiorite	193.0 ± 1.0	LA-ICP-MS	[88]
151	1094-1	44°56'03"	128°32'51"	Yabuli	Monzogranite	201.0 ± 2.0	LA-ICP-MS	[88]
152	1106-1	44°55'11"	128°44'12"	Shangyuchi	Monzogranite	195.0 ± 2.0	LA-ICP-MS	[88]
153	1106-1	44°55'11"	128°44'12"	Shangyuchi	Monzogranite	183.0 ± 1.0	LA-ICP-MS	[88]
154	1111-1	44°56'01"	128°54'31"	Shangkaidatun	Monzogranite	196.0 ± 1.0	LA-ICP-MS	[88]
155	1118-1	44°46'22"	128°35'54"	Baoshancun	Monzogranite	202.0 ± 1.0	LA-ICP-MS	[88]
156	1092-1	44°57'16"	128°29'42"	Shangguoshuchang	Biotite syenite granite	202.0 ± 1.0	LA-ICP-MS	[88]
157	1094-2	44°56'03"	128°32'53"	Shangliuhe	Biotite syenite granite	197.0 ± 1.0	LA-ICP-MS	[88]
158	1090-4	44°57'32"	128°25'48"	Shangweihe	Syenite granite	191.0 ± 1.0	LA-ICP-MS	[88]
159	BMG	47°32'	128°32'	Luming	Biotite monzogranite	187.5 ± 2.8	LA-ICP-MS	[89]
160	MG	47°32'	128°32'	Luming	Monzogranite	186.5 ± 3.6	LA-ICP-MS	[89]
161	PG	47°32'	128°32'	Luming	Monzogranite	178.6 ± 2.2	LA-ICP-MS	[89]
162	GP	47°32'	128°32'	Luming	Granite porphyry	177.4 ± 3.0	LA-ICP-MS	[89]
163	SG	47°32'	128°32'	Luming	Syenogranite	175.6 ± 3.0	LA-ICP-MS	[89]
164	STH-1	44°52'22"	128°40'26"	Shihe	Monzogranite	201.0 ± 2.0	LA-ICP-MS	[90]
165	STH-2	44°51'43"	128°42'30"	Shihe	Tonalite	198.0 ± 3.0	LA-ICP-MS	[90]
166	STH-2E	44°51'43"	128°42'30"	Shihe	Mafic enclaves	196.0 ± 3.0	LA-ICP-MS	[90]
167	1074TW			Dongxintun	Quartz diorite	176.2 ± 1.8	LA-ICP-MS	[91]
168	014-1-TW01			Dongxintun	Granodiorite	182.4 ± 1.1	LA-ICP-MS	[91]
169	014-1-TW02			Dongxintun	Monzonitic granite	172.7 ± 1.6	LA-ICP-MS	[91]
170	DB07TW			Dongxintun	Black cloud quartz diorite	168.2 ± 0.4	LA-ICP-MS	[91]
171	3082TW			Dongxintun	Syenite granite	166.0 ± 2.2	LA-ICP-MS	[91]
172	S1	45°41'39"	127°29'33"	Taipingqiao	Monzonitic granite	177.0 ± 1.0	LA-ICP-MS	[92]
173	S5	45°38'55"	127°40'26"	Yujiatun	Syenogranite	185.0 ± 1.0	LA-ICP-MS	[93]
174	S8	46°07'20"	127°33'04"	Zhaojiadian	Syenogranite	177.0 ± 1.0	LA-ICP-MS	[93]
175	S12	46°14'44"	127°27'42"	Guoyongfatun	Monzonitic granite	176.0 ± 2.0	LA-ICP-MS	[93]
176	S13	46°18'09"	127°28'54"	Zhendongcun	Two-mica granite	232.0 ± 2.0	LA-ICP-MS	[93]
177	S15	46°29'50"	127°41'59"	Xi'ertun	Granodiorite	174.0 ± 1.0	LA-ICP-MS	[93]
178	S16	46°55'09"	128°11'01"	Tieli	Monzonitic granite	186.0 ± 2.0	LA-ICP-MS	[93]
179	S17	45°39'41"	127°10'32"	Jijiatuan	Granite	173.0 ± 3.0	LA-ICP-MS	[93]
180	S21	45°25'59"	128°27'54"	Fushantun	Granite	185.0 ± 2.0	LA-ICP-MS	[93]
181	S24	46°11'59"	128°35'18"	Chuankoucun	Granite	195.0 ± 3.0	LA-ICP-MS	[93]
182	PM011-62	43°46'07"	127°11'01"	Laoyeling	Granodiorite	190.0 ± 0.4	LA-ICP-MS	[94]
183	PM011-36	43°47'26"	127°10'54"	Songjiacun	Monzogranite	192.4 ± 0.9	LA-ICP-MS	[94]
184	PM007-51	43°42'13"	127°06'10"	Dadingzi	Monzogranite	187.0 ± 2.3	LA-ICP-MS	[94]
185	D6321	43°48'35"	127°18'01"	Dadianzi	Alkali feldspar granite	192.1 ± 1.7	LA-ICP-MS	[94]
186	P314	47°20'54"	129°36'22"	Fengmao forest farm	Monzogranite	211.0 ± 1.0	LA-ICP-MS	[95]
187	P244	47°24'53"	129°40'57"	Fengmao forest farm	Granite porphyry	210.0 ± 2.0	LA-ICP-MS	[95]
188	P10-2	47°22'51"	129°59'27"	Sihao forest farm	Granodiorite	244.0 ± 2.0	LA-ICP-MS	[95]
189	P3LT43	47°29'01"	129°59'10"	530 forest farm	Granodiorite	182.0 ± 2.0	LA-ICP-MS	[96]
190	P1LT92	47°05'11"	128°50'41"	Nanchaolin	Monzogranite	175.0 ± 3.0	LA-ICP-MS	[97]
191	CP9LT10	47°13'01"	128°50'31"	Hangyuelin	Monzogranite	195.0 ± 2.0	LA-ICP-MS	[97]
192	FAP-N1	44°27'	127°20'	Fu'anpu	Monzogranite	172.5 ± 0.8	LA-ICP-MS	[98]
193	FAP-N2	44°24'	127°15'	Fu'anpu	Granodiorite	172.8 ± 1.1	LA-ICP-MS	[98]
194	YZ02-7	42°55'56"	128°42'29"	Mengshan	Granodiorite	181.0 ± 2.0	LA-ICP-MS	[99]

Table 3. Cont.

Order	Sample	Latitude	Longitude	Location	Lithology	Age (Ma)	Method	Reference
195	YZ02-5	42°54'49"	128°43'20"	Mengshan	Monzogranite	174.0 ± 3.0	LA-ICP-MS	[99]
196	YZ02-10	42°49'58"	128°53'40"	Mengshan	Granodiorite	184.0 ± 2.0	LA-ICP-MS	[99]
197	YZ02-2	42°51'15"	128°30'32"	Dakai	Monzogranite	249.0 ± 4.0	LA-ICP-MS	[99]
198	FW00-37	42°52'01"	128°02'30"	Huangniling	Monzogranite	168.0 ± 3.0	TIMS	[99]
199	FW00-40	42°55'12"	127°38'11"	Huangniling	Granodiorite	171.0 ± 5.0	TIMS	[99]
200	YZ02-33	42°27'53"	129°15'20"	Gaoling	Granodiorite	170.0 ± 3.0	LA-ICP-MS	[99]
201	YZ02-45	42°37'16"	129°12'01"	Gaoling	Monzogranite	192.0 ± 2.0	LA-ICP-MS	[99]
202	YZ02-12-3	42°28'46"	128°56'12"	Bailiping	Tonalite	285.0 ± 9.0	LA-ICP-MS	[99]
203	YZ02-22-2	42°12'14"	128°49'21"	Bailiping	Monzogranite	245.0 ± 6.0	LA-ICP-MS	[99]
204	YZ02-25-2	42°10'57"	128°44'58"	Bailiping	Monzogranite	245.0 ± 3.0	LA-ICP-MS	[99]
205	YZ02-27-2	42°03'10"	128°49'32"	Bailiping	Monzogranite	248.0 ± 2.0	LA-ICP-MS	[99]
206	YZ02-28	42°04'19"	128°54'16"	Bailiping	Diorite	178.0 ± 2.0	LA-ICP-MS	[99]
207	YZ02-16-1	42°21'58"	128°39'38"	Bailiping	Syenogranite	187.0 ± 3.0	LA-ICP-MS	[99]
208	YZ02-18-3	42°20'20"	128°50'15"	Bailiping	Granodiorite	119.0 ± 2.0	LA-ICP-MS	[99]
209	YZ02-21-1	42°13'34"	128°47'55"	Bailiping	Quartz diorite	116.0 ± 1.0	LA-ICP-MS	[99]

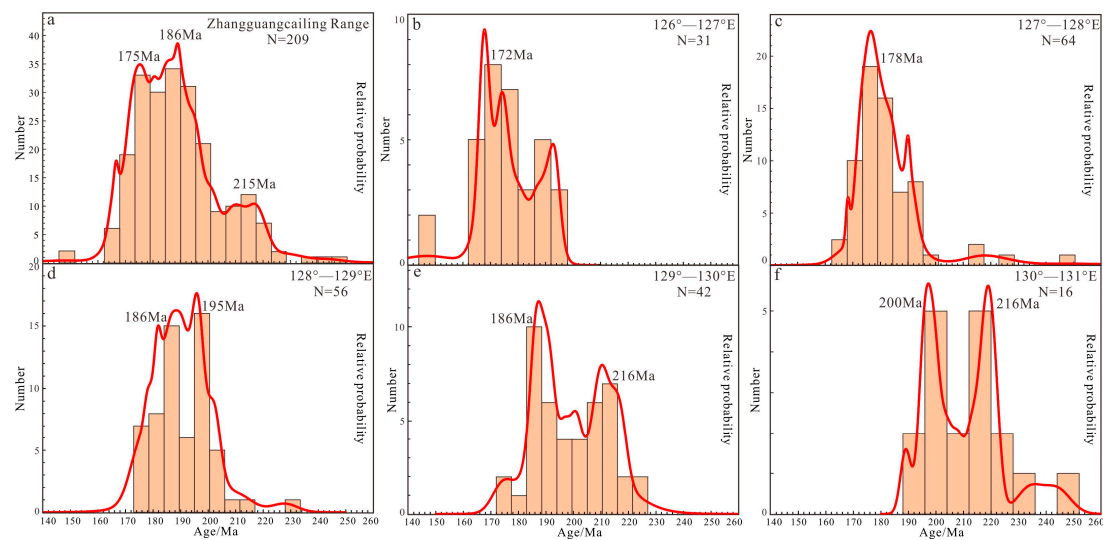
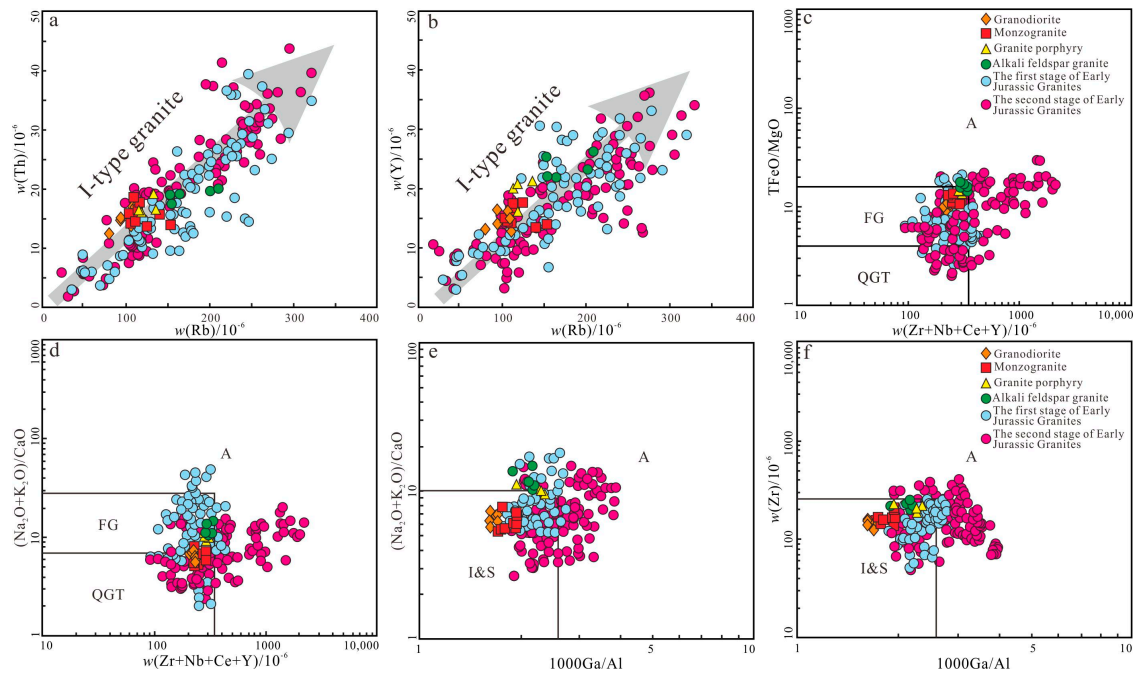


Figure 7. Frequency distribution diagram of zircon U-Pb ages of Early to Middle Mesozoic intrusive rocks in the Lesser Xing'an–Zhangguangcai Range (a–f).

### 5.2. Granite Genesis Types

The Early Jurassic granitoids in the Yangmugang area belong to the weakly peraluminous–peraluminous high-K calc-alkaline series of rocks. They exhibit characteristics (Figure 5) such as high silicon and aluminum contents; an elevated alkali content; low magnesium, phosphorus, and titanium contents; and a high TFeO/MgO ratio (with an average value of 12.66) [6,8,11]. The rock contains visible biotite and common hornblende, with accessory minerals that include magnetite and apatite. It is notably different from S-type granites, which are strongly aluminum-rich (containing minerals such as garnet and muscovite) and characterized by an A/CNK > 1.1 [49]. Furthermore, in the Rb–Th diagram (Figure 8a) and Rb–Y diagram (Figure 8b), a positive correlation between the Th and Y contents with the Rb content was observed, indicating the characteristics of type I granites [50–52]. In the (Zr + Nb + Ce + Y)–(TFeO/MgO) diagram (Figure 8c) and the (Zr + Nb + Ce + Y)–(Na<sub>2</sub>O + K<sub>2</sub>O)/CaO diagram (Figure 8d), the granodiorite and monzonitic granite samples fell into the I-type granite zone and the granite porphyry and alkali feldspar granite samples fell into the transitional zone between highly fractionated, high-silica granitic rocks and A-type granites. In the 1000Ga/Al–(Na<sub>2</sub>O + K<sub>2</sub>O)/CaO diagram (Figure 8e) and the 1000Ga/Al–w(Zr) diagram (Figure 8f), the rock samples fell into the transitional zone between I-type granites and A-type granites. The Zr/Hf values effectively reflect the degree of magmatic differentiation. The Zr/Hf values can categorize granites into highly fractionated granites

(<25), moderately fractionated granites (25–55), and typical granites (>55) [53]. In this study, the average Zr/Hf ratios for the Early Jurassic granodiorite, monzonitic granite, granite porphyry, and alkali feldspar granite samples were 26.72, 22.46, 20.46, and 17.84. These samples also exhibited high differentiation indices, with  $I_D$  values of 85.64, 89.26, 93.14, and 97.26. This indicates that the Early Jurassic granodiorite is moderately fractionated granite, while the monzonitic granite, granite porphyry, and alkali feldspar granite have undergone significant differentiation processes.



**Figure 8.** Rb–Th diagram (a), Rb–Y diagram (b) (a,b modified from [50–52]), (Zr + Nb + Ce + Y)–TFeO/MgO diagram (c), (Zr + Nb + Ce + Y)–(Na<sub>2</sub>O + K<sub>2</sub>O)/CaO diagram (d), 1000 Ga/Al–(Na<sub>2</sub>O + K<sub>2</sub>O)/CaO diagram (e) (c–e modified from [51]), and 1000 Ga/Al–(Zr) diagram (f) (modified from [16]) of Late Jurassic granitoids from the Yangmugang area in the Lesser Xing’an–Zhangguangcai Range. FG: fractionated granite; OGT: unfractionated M-, I-, and S-type granite.

In addition, the research area’s Early Jurassic granitoids exhibited the following characteristics: (1) Compared to A-type granite, highly differentiated I-type granite has a lower total rare earth element content ( $\Sigma\text{REE} < 150 \times 10^{-6}$ ). The average  $\Sigma\text{REE}$  content of the granite samples in this study was  $135.99 \times 10^{-6}$  ( $< 150 \times 10^{-6}$ ), which is consistent with the characteristics of highly differentiated I-type granite. (2) Highly differentiated I-type granite has lower contents of Zr, Nb, Ce, and Y. The average value of Nb + Zr + Y + Ce in the granite samples in this study was  $267.13 \times 10^{-6}$ , which was lower than the minimum value for A-type granite ( $350 \times 10^{-6}$ ) [51]. (3) The average 1000 Ga/Al ratios for the Early Jurassic granodiorite, monzonitic granite, granite porphyry, and alkali feldspar granite samples were 1.67, 1.86, 2.22, and 2.12, which were close to the average 1000 Ga/Al ratio of highly differentiated I-type granites (2.10) and lower than the average 1000 Ga/Al ratio of A-type granites (3.75) [16]. (4) In this study, the average zircon saturation temperature ( $T_{\text{Zr}}$ ) for the Early Jurassic granodiorite, monzonitic granite, granite porphyry, and alkali feldspar granite samples were 770 °C, 783 °C, 794 °C, and 793 °C, a bit lower than the zircon saturation temperature of A-type granites (800 °C) [17]. In summary, the Early Jurassic granodiorite in the study area was classified as moderately differentiated I-type granite, while the monzonitic granite, granite porphyry, and alkali feldspar granite were categorized as highly differentiated I-type granites.

### 5.3. Magmatic Source Characteristics

There is still controversy surrounding the origin of I-type granites, and several different viewpoints exist: (1) the partial melting of mantle material and fractional crystallization processes [54]; (2) the mixing of mantle-derived basaltic magma and crustal-derived granitic magma [16,17,55]; and (3) the partial melting of lower crustal mafic rocks [56]. Magma formed by the partial melting of mantle material is typically mafic-neutral and is characterized by a lower SiO<sub>2</sub> content and high Mg<sup>#</sup> values (Mg<sup>#</sup> > 65) [57]. The Early Jurassic granitoids in the study area had a high SiO<sub>2</sub> content and low Mg<sup>#</sup> values (Mg<sup>#</sup> = 10–20), which do not match the geochemical characteristics of granitoids formed by the partial melting of mantle-derived magmas (Mg<sup>#</sup> > 65). Instead, they exhibit geochemical similarities to granitoids formed by the partial melting of the lower crust (Mg<sup>#</sup> < 40). Furthermore, the Early Jurassic granitoids studied in this research are widely distributed in the Lesser Xing'an–Zhangguangcai Range, forming a massive NS-trending magmatic belt. Such a large-scale acidic magmatic belt is less likely to have formed through the crystallization and differentiation of mantle-derived magmas. Furthermore, in the Early Jurassic granitoids of the Yangmugang area, no iron–magnesium-rich inclusions were found, indicating that the magma source for the Early Jurassic granitoids in the Yangmugang area is less likely to have resulted from crust–mantle mixing.

The Early Jurassic granitoids in the study area are characterized by high silica, high potassium, high alkalinity, low iron, low magnesium, low calcium, and low titanium contents. They are enriched in large-ion lithophile elements and depleted in high-field-strength elements, which is consistent with a rock genesis model involving the partial melting of the lower crust [43]. The distribution pattern of trace elements and rare earth elements (Figure 6) was similar to the distribution pattern of the lower continental crust and large continental blocks. This suggests characteristics of a crustal origin. The Early Jurassic granitoid samples in the study area had Nb/Ta values of 8.20–17.24 (with an average of 11.08) and Rb/Sr values of 0.28–0.99 (with an average of 0.51). These values are relatively close to the average chemical composition of crustal rocks (Nb/Ta = 11.4, Rb/Sr = 0.35) [55,58]. The values of Ti/Y and Ti/Zr were 28.85–183.33 (with an average of 103.35) and 3.33–20 (with an average of 10.07). These values fell within the range typical of crustal-source magmas (Ti/Y < 200 and Ti/Zr < 30) [46,58]. Furthermore, the Early Jurassic granitoid samples in the study area were positioned within the crustal source range in the  $\delta\text{Eu}-(\text{La}/\text{Yb})_{\text{N}}$  diagram (Figure 9a), within the continental upper crustal region in the Nb/Y–Th/Y diagram (Figure 9b) and within the upper crustal region in the Ta/Yb–Th/Yb diagram (Figure 9c). They exhibited a trend indicative of fractional crystallization evolution, further indicating that the source magma for the Early Jurassic granitoids in the study area originated from the partial melting of crustal materials. The depletion of Ba, Sr, and Eu suggests that a process of plagioclase accumulation may have occurred during the partial melting of crustal materials [59,60], and the low  $(\text{La}/\text{Yb})_{\text{N}}$  values (6.48–10.43), along with high Yb (1.77–3.14) and Y (9.20–19.10) values, indicate the absence of garnet in the magma source region. Furthermore, based on mineral thermobarometry experiments [61,62], the pressure at which plagioclase disappears is 1.2 GPa, while garnet formation occurs at pressures between 0.8 and 1.0 GPa. Therefore, it can be inferred that the Early Jurassic granitoids in the study area formed at pressures of less than 0.8 GPa, corresponding to an estimated burial depth of less than 30 km based on simulation calculations.

Based on previous Early Jurassic granitoids in the Yangmugang area of the Lesser Xing'an Range by predecessors [16,44,63], the  $(^{87}\text{Sr}/^{86}\text{Sr})_{\text{i}}$  values of the granite within the area are 0.704133–0.704740, the  $\varepsilon_{\text{Nd}}(t)$  values are  $+0.2 \pm 5.91$ , the  $T_{\text{DM2}}$  values are 0.75–0.98 Ga, and the positive  $\varepsilon_{\text{Nd}}(t)$  values and relatively younger model ages ( $T_{\text{DM2}}$ ) suggest that the source rocks originated from the melting of mafic lower crustal materials of a Mesoproterozoic to Neoproterozoic age. This is consistent with the geochemical characteristics and  $\varepsilon_{\text{Hf}}(t)$  values of several granite bodies in the Early Jurassic section of the Lesser Xing'an Range [26,44,64]. Furthermore, previous research suggests that the  $\varepsilon_{\text{Nd}}(t)$  values and  $T_{\text{DM2}}$  variations in the granite of the eastern margin of the Xingmeng Orogenic

Belt show little change, implying that rocks of different ages and types in this area may have originated from a similar source region [65,66]. In summary, this study concludes that the Early Jurassic granitoid magmas in the Yangmugang area originated from the partial melting of lower crustal materials.

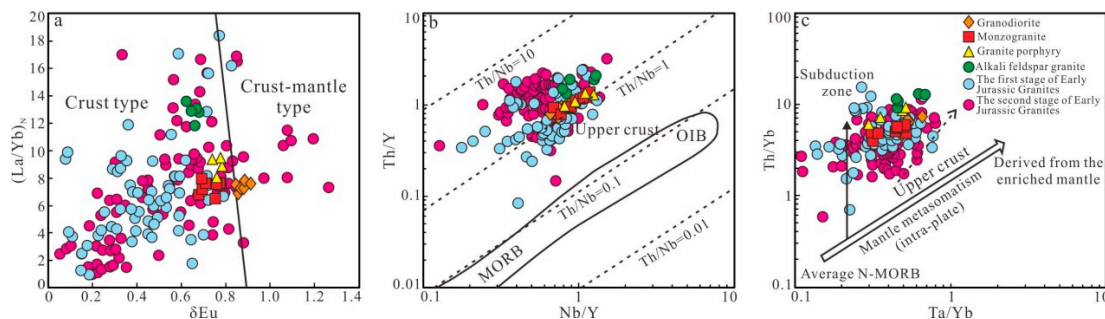


**Figure 9.**  $\delta\text{Eu}-(\text{La}/\text{Yb})_N$  diagram (a) (modified from [67]),  $\text{Nb}/\text{Y}-\text{Th}/\text{Y}$  diagram (b) (modified from [68]), and  $\text{Ta}/\text{Yb}-\text{Th}/\text{Yb}$  diagram (c) (modified from [69]) of Late Jurassic granitoids from the Yangmugang area in the Lesser Xing'an–Zhangguangcai Range.

#### 5.4. Granite's Evolutionary Characteristics

In the study area, during the Early Jurassic period, the  $\text{SiO}_2$  content and total alkali content ( $\text{Na}_2\text{O} + \text{K}_2\text{O}$ ) gradually increased in granodiorite, monzonitic granite, granodiorite porphyry, and alkali feldspar granite. Conversely, the contents of  $\text{Fe}_2\text{O}_3$ ,  $\text{FeO}$ , and  $\text{MgO}$  decreased with an increase in the silica content, indicating the evolution of magma towards the acidic direction. The low Ba values in the rock indicate intense fractional crystallization of the magma, while the high  $I_D$  values (85.64–97.26) and low Zr/Hf values (15.18–28.77) indicate a high degree of magmatic differentiation and evolution. As the magmatic differentiation process proceeds from granodiorite to alkali feldspar granite, the granite in this period is primarily characterized by compositional evolution, featuring high silica, high alkali, low iron, low magnesium, and low calcium contents. The granite samples exhibited increasing  $I_D$  values, A/CNK values, and Rb/Sr values, while the  $I_S$  values and Zr/Hf values gradually decreased [70]. This reflects that, for granodiorite–monzonitic granite–granodiorite porphyry–alkali feldspar granite, the degree of magma differentiation and evolution becomes progressively higher, indicating a more thorough evolution.

In the Harker diagram (Figure 10), there is a strong linear relationship between the  $\text{SiO}_2$  content and the content of other oxides, indicating that the granodiorite, monzonitic granite, granodiorite porphyry, and alkali feldspar granite samples originated from the same or a similar source region. From granodiorite to alkali feldspar granite, as the  $\text{SiO}_2$  content increased, the contents of  $\text{Al}_2\text{O}_3$ ,  $\text{TiO}_2$ , TFeO,  $\text{MgO}$ ,  $\text{CaO}$ ,  $\text{MnO}$ , and  $\text{P}_2\text{O}_5$  gradually decreased. While the  $\text{K}_2\text{O}$  content increased gradually, the  $\text{Na}_2\text{O}$  content remained relatively constant. It is evident that the fractional crystallization of dark-colored minerals plays a significant role in the magma evolution process. This further increases the total alkali content in the rock, indicating an overall trend of evolution from weakly peraluminous to peraluminous characteristics in the rock. Furthermore, the granodiorite to alkali feldspar granite samples, as depicted in the granite petrogenesis discrimination diagrams proposed in Figure 8c–e, show that, with increasing magma differentiation and evolution, the rocks exhibited a trend of evolving from weakly peraluminous middle-differentiated I-type granite towards peraluminous high-differentiated I-type.

The Early Jurassic granitoid samples in the study area exhibited a right-skewed distribution in the rare earth element partition diagrams, which was characterized by enrichment in light rare earth elements and depletion in heavy rare earth elements (Figure 6a). The evolution of Eu shows a transition from weakly negative anomalies to stronger negative anomalies (Figure 6a). The identification diagrams Ba–Rb (Figure 11a) and Ba–Sr (Figure 11b) show that the loss of Sr, Ba, and Eu and the enrichment of Rb in the rock mass

were mainly caused by the crystallization differentiation of potassium feldspar and anorthoclase (Figure 11a,b) [16,17]. The depletion of P and Ti was likely a result of the fractional crystallization of accessory minerals such as apatite and Fe-Ti minerals (Figure 11c). The depletion of Ba, Sr, and Nd further supports the evident mineral fractional crystallization during the magma evolution process.

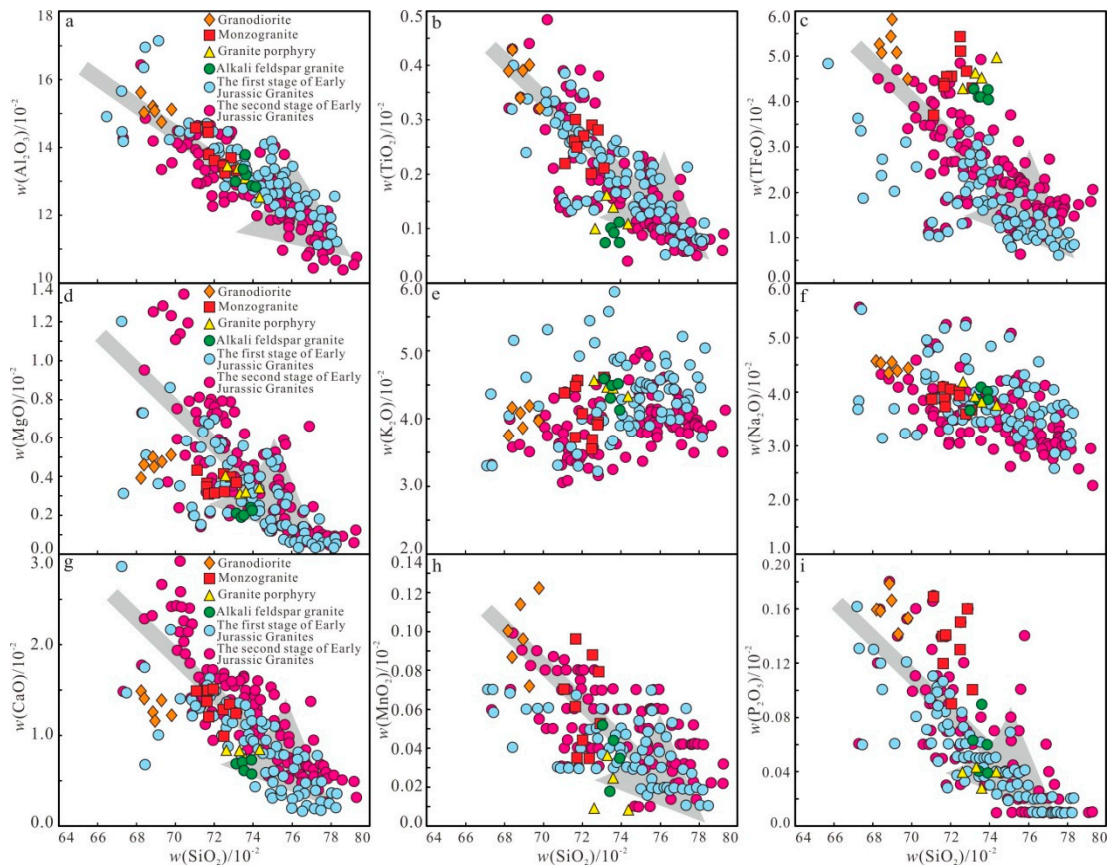


**Figure 10.** Harker diagrams of Late Jurassic granitoids from the Yangmugang area in the Lesser Xing’an—Zhangguangcai Range. (a) SiO<sub>2</sub>-Al<sub>2</sub>O<sub>3</sub> correlation diagram; (b) SiO<sub>2</sub>-TiO<sub>2</sub> correlation diagram; (c) SiO<sub>2</sub>-TFeO correlation diagram; (d) SiO<sub>2</sub>-MgO correlation diagram; (e) SiO<sub>2</sub>-K<sub>2</sub>O correlation diagram; (f) SiO<sub>2</sub>-Na<sub>2</sub>O correlation diagram; (g) SiO<sub>2</sub>-CaO correlation diagram; (h) SiO<sub>2</sub>-MnO correlation diagram; (i) SiO<sub>2</sub>-P<sub>2</sub>O<sub>5</sub> correlation diagram.

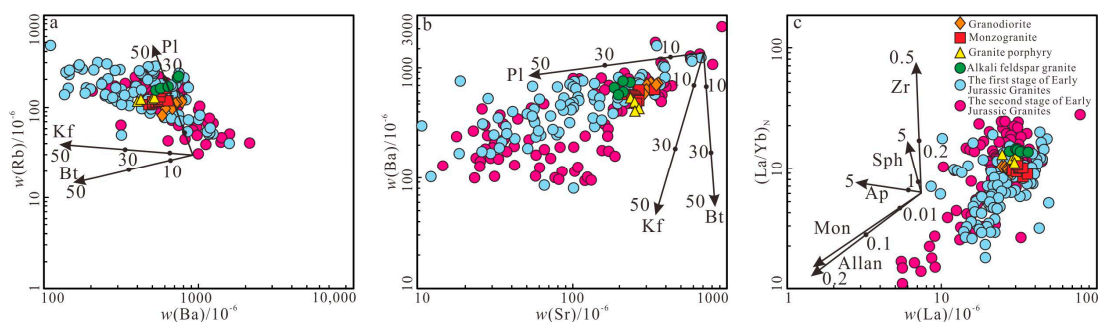


**Figure 11.** Ba-Rb diagram (a) (modified from [71]), Sr-Ba diagram (b), and La- (La/Yb)<sub>N</sub> diagram (c) (b,c modified from [16]) of Late Jurassic granitoids from the Yangmugang area in the Lesser Xing’an—Zhangguangcai Range.



### 5.5. Implications for the Evolution of the Mudanjiang Ocean

The late Early Jurassic granitoid samples in the study area were characterized by high silica, high potassium, high alkalinity, low iron, low magnesium, low calcium, and low titanium contents, making them high-K calc-alkaline rocks. Their A/CNK value was generally less than 1.1, indicating weakly peraluminous to peraluminous rocks. Their trace element composition showed enrichment in large-ion lithophile elements and light rare earth elements, as well as depletion in high-field-strength elements, classifying them as high-K calc-alkaline type I granites. Previous studies have indicated that high-K calc-alkaline granites can form in tectonic settings such as active continental margins and post-orogenic environments [68,72,73]. The granitoid samples in the study area, as depicted in the (Yb + Ta)-Rb diagram (Figure 12a), fell within the volcanic arc granite field; in the (Y + Nb)-Rb diagram (Figure 12b), they fell within the post-collisional granite field; and in the  $R_1$ - $R_2$  diagram (Figure 12c), they fell within the late orogenic granite field. In the  $\text{SiO}_2$ -lgCaO/(K<sub>2</sub>O + Na<sub>2</sub>O) diagram (Figure 12d), they fell into the overlapping boundary line of the compressional types and extensional types. In the Yb-Sr diagram (Figure 12e), the magma fell into the low-Sr high-Yb-type granite area, with a few falling into the low-Sr low-Yb-type granite area. According to the classification, we can conclude that the parent magma came from the shallow low-pressure extension background (<0.8 or 1.0 GPa) [78]. In the  $\text{SiO}_2$ -Al<sub>2</sub>O<sub>3</sub> diagram (Figure 12f), the parent magma fell into the post-orogenic granite area. To sum up, the late Early Jurassic granites in the research area were formed in the late orogenic tectonic environment.

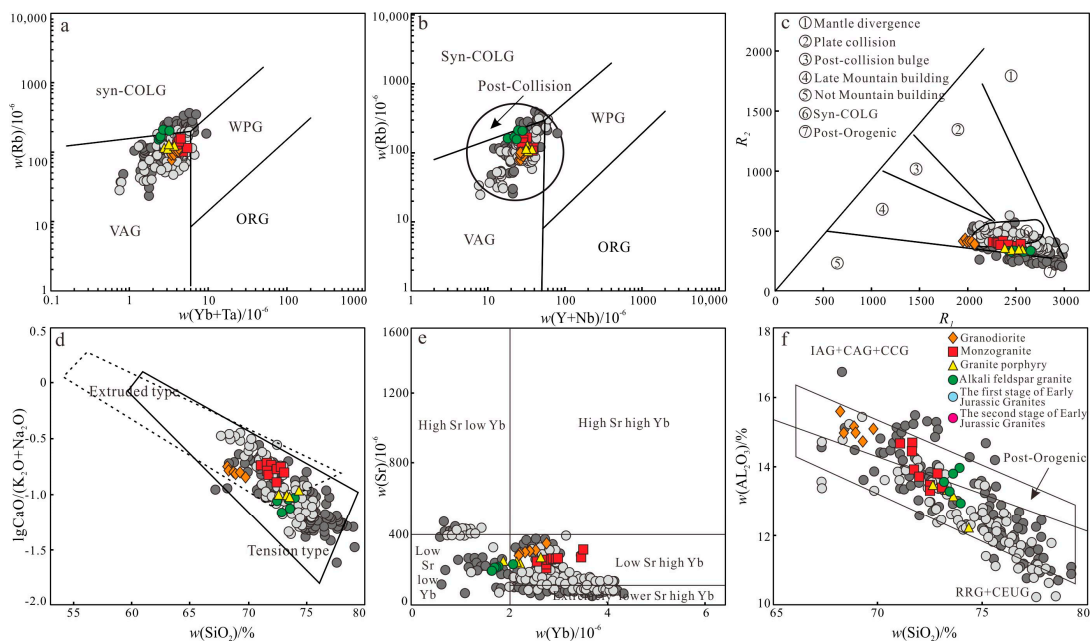


**Figure 12.** (Yb + Ta)-(Rb) diagram (a), (Y + Nb)-(Rb) diagram (b) (modified from [50]),  $R_1$ - $R_2$  diagram (c) (modified from [74]),  $\text{SiO}_2$ -lgCaO/(K<sub>2</sub>O + Na<sub>2</sub>O) diagram (d), Yb -Sr diagram (e), and  $\text{SiO}_2$ -Al<sub>2</sub>O<sub>3</sub> diagram (f) of Late Jurassic granitoids from the Yangmugang area in the Lesser Xing'an-Zhangguangcai Range.

Based on the research findings of previous scholars, it is widely recognized that the late Early Jurassic Lesser Xing'an-Zhangguangcai Range is situated in an extensional tectonic environment [4,8,9]. However, there is still considerable debate about the specific tectonic regime that influenced it. Previous research results have indicated that the closure of the ancient Asian Ocean and the ultimate collision between the Xingmeng Orogenic Belt and the North China Craton occurred during the Middle-Late Triassic period [75-77], forming a magmatic belt that extends east to west along the Changchun-Yanji suture zone [68]. The granitoid formation age in the study area was 182.9-177.2 Ma, and the magmatic belt

in the Lesser Xing'an–Zhangguangcai Range, including the study area, is oriented in a north–south direction. Therefore, during the late Early Jurassic, the influence of the tectonic system related to the ancient Asian Ocean on the Lesser Xing'an–Zhangguangcai Range, including the study area, appears to have been limited.

Furthermore, to the west of the Songnen–Zhangguangcai Range block, there are Early Jurassic granitoids belonging to the medium- to high-K calc-alkaline series, exhibiting geochemical characteristics of type I granites [2,10–12,62–65]. These granitoids are believed to have formed in an active continental margin volcanic island arc environment and are associated with the southward subduction of the Mongol–Okhotsk Ocean [48,65]. The late Early Jurassic granitoids exposed in the Songnen–Zhangguangcai Range block, including the study area, belong to the high-K calc-alkaline series and were formed in a late orogenic extensional tectonic environment [28–30]. The Early Jurassic granitoids to the west of the Songnen block exhibit a distinctly different tectonic environment compared to the Early Jurassic granitoids in the Songnen block and its eastern regions [2,21,22,25,26]. This indicates that, during the late Early Jurassic, the influence of the Mongol–Okhotsk Ocean on the Lesser Xing'an–Zhangguangcai Range, including the study area, was limited [27,29,30]. Therefore, considering the regional tectonic background, this study suggests that the late Early Jurassic granitoids in the Lesser Xing'an–Zhangguangcai Range, including the study area, were formed in a late orogenic extensional tectonic environment. This formation was likely related to the collision and closure of the Mudanjiang Ocean and the westward subduction of the ancient Pacific Plate. This conclusion can be further supported by the following aspects (Figure 13):

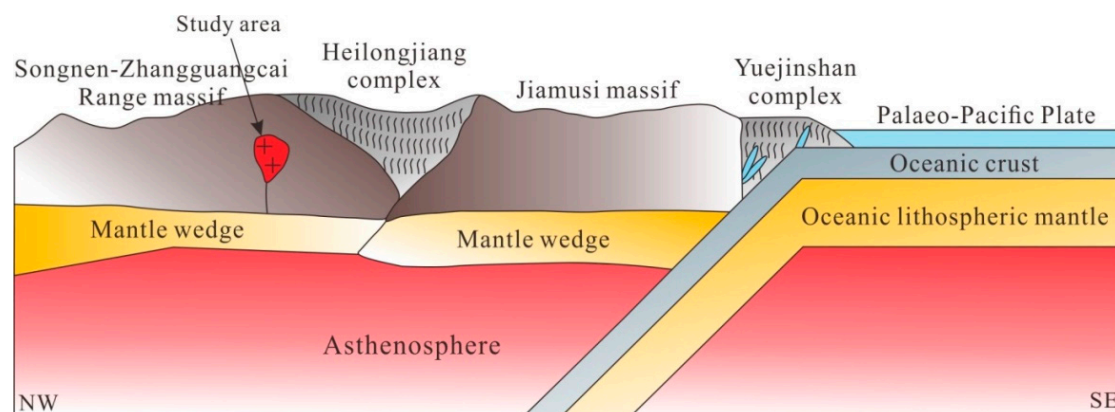


**Figure 13.** Early Jurassic Toarian tectonic evolution diagram of the Yangmugang area in the Lesser Xing'an–Zhangguangcai Range.

The eastern margin of the Songnen–Zhangguangcai Range block and the western margin of the Jiamusi block are characterized by a north–south-trending Permian granite belt. This belt consists of high-potassium calc-alkaline rocks that exhibit enrichment in light rare earth elements (LREEs) and large-ion lithophile elements (LILEs) while showing depletion in heavy rare earth elements (HREEs) and high-field-strength elements (HFSEs). These geochemical characteristics are similar to those of subduction-zone magmatic rocks [11,22,78]. Additionally, the Middle Permian ultramafic rocks in the Dajindingzi, Zhushan, and Xinnangou areas along the Mudanjiang suture zone display active continental margin attributes and geochemical characteristics of ocean island basalts (OIBs), mid-ocean ridge basalts (MORBs), and arc basalts [29]. The Heilongjiang blueschists (288–258 Ma) also show geochemical attributes of OIBs, MORBs, and arc basalts [11], indicating that they formed in an oceanic island environment [15,79]. This evidence suggests that the Mudanjiang Ocean experienced bidirectional subduction during the Early Permian period.

During the Triassic period, the Yilan region developed metamorphic basalts with OIB characteristics (251–243 Ma), while the Mudanjiang region developed plagioclase amphibolites with N-MORB characteristics (284.0 Ma) and blueschists with E-MORB characteristics

(224–213 Ma) [15], indicating that the Mudanjiang Ocean had not closed by the Late Triassic period [14,40,47]. Additionally, a small amount of I-type granite related to oceanic crust subduction (250–246 Ma) was found in the Fuxing Forest Farm at the western margin of the Jiamusi block [80]. In the eastern margin of the Songnen–Zhangguangcai Range block, the Pingdingshan monzogranite (249.8 Ma) and the Lianzhushan monzogranite (243.7 Ma), which exhibited arc magmatic rock characteristics, are related to the subduction of the Mudanjiang Ocean [81]. Furthermore, in the Gaogangshan area of the Lesser Xing’an Range, granitic porphyry (247.6 Ma) associated with porphyry copper–molybdenum deposits developed [78]. This highly differentiated I-type granite showed chemical characteristics of syn-collisional granites and is related to the rollback of the westward-subducting plate of the Mudanjiang Ocean between the Songnen–Zhangguangcai Range block and the Jiamusi block. During the Triassic period, the Mudanjiang Ocean basin shrank and bidirectional subduction continued.

Previous studies have determined the  $^{40}\text{Ar}$ – $^{39}\text{Ar}$  ages of metamorphic muscovite from single minerals in the accretionary complex of the Mudanjiang Ocean, with the metamorphic ages concentrated between 185 and 165 Ma [15,26,53]. This metamorphic peak is believed to postdate the initial collision between the Songnen–Zhangguangcai Range block and the Jiamusi block and is considered the closure time of the Mudanjiang Ocean [11]. Dong [13] obtained a rutile cooling age of 177 Ma from amphibolite in the accretionary complex of the Yilan region, while Zhao et al. [82] obtained an age of 177 Ma for felsic mylonite in the Huanan region. This deformation event, characterized by the transition from high-P-T metamorphic mineral assemblages to low-P-T metamorphic mineral assemblages, is interpreted as the exhumation process of deep metamorphic assemblages to shallower levels following the collision and closure of the Songnen–Zhangguangcai Range block and the Jiamusi block [28,40,48,83–85]. These geological events indicate that the region underwent significant tectono-thermal events during the Early to Middle Jurassic period, leading to the closure of the Mudanjiang Ocean and the rapid uplift of the accretionary complex.

In the Early Jurassic period, the Lesser Xing’an–Zhangguangcai Range developed typical bimodal igneous rocks, exhibiting compositional zoning parallel to the Northeast Asian continental margin [86]. Concurrently, a calc-alkaline igneous assemblage developed in eastern Jilin and Heilongjiang, displaying a northeast–southwest-trending belt. From west to east, the  $\text{SiO}_2$  and  $\text{K}_2\text{O}$  contents gradually increase, while the  $\epsilon_{\text{Nd}}(t)$  values gradually decrease [29,85], indicating the initiation of the subduction of the Paleo-Pacific tectonic system during the Early Jurassic period [87–89]. By the late Early Jurassic period, an ultramafic–mafic intrusive rock belt (186–182 Ma) was discovered in the Yichun–Tieli–Shangzhi area [14,15,22,88,90–92]. This mafic rock belt is believed to be related to large-scale mantle-derived magma underplating in an extensional setting [88,93,94], forming a typical bimodal igneous assemblage with contemporaneous I-type and A-type granites in the region [27,95,96]. This process is possibly associated with the subduction rollback of the Paleo-Pacific. Additionally, the EW-directed thrust structures along the eastern margin of the Songnen–Zhangguangcai Range block [5,43,97] and the nearly NS distribution of the Mudanjiang accretionary complex after tectonic exhumation [17,86,98,99] suggest that the closure of the Mudanjiang Ocean and the uplift of the accretionary complex may be related to the subduction of the Paleo-Pacific beneath the eastern margin of the Eurasian continent.

In summary, considering the regional tectonic evolution and the late Early Jurassic (182.9–177.2 Ma) granitoids in the study area within a post-orogenic extensional setting, it was concluded that the granitoids in the study area are products of the extensional environment following the collision of the Songnen–Zhangguangcai Range block and the Jiamusi block along the Mudanjiang suture zone. This further constrains the complete closure of the Mudanjiang Ocean to the late Early Jurassic period.

## 6. Conclusions

1. The intrusion ages of the granodiorite, monzonitic granite, granodiorite porphyry, and alkali feldspar granite in the Yangmugang area of the Lesser Xing’an–Zhangguangcai

Range were  $182.9 \pm 1.4$  Ma,  $180.8 \pm 0.9$  Ma,  $177.8 \pm 1.6$  Ma, and  $177.2 \pm 2.2$  Ma. These ages collectively represent products of the late Early Jurassic magmatic evolution event.

2. The late Early Jurassic granitoids in the study area are characterized by high silicon and aluminum contents, a high alkalinity, and low magnesium, phosphorus, and titanium contents, as well as a high TFeO/MgO ratio. The granodiorite belongs to the moderately differentiated I-type granitoids, while the monzonitic granite, granodiorite porphyry, and alkali feldspar granite belong to the highly differentiated I-type granites. The magma source for these granitoids was derived from the melting of lower crustal material from the Mesoproterozoic to the Neoproterozoic eras.

3. In the study area, there is a progression from granodiorite to alkali feldspar granitoids. This sequence represents an increasing degree of magmatic differentiation and exhibits a trend towards evolving from weakly peraluminous middle-differentiated I-type granitoids towards peraluminous high-differentiated I-type.

4. The late Early Jurassic granitoids in the study area formed in an extensional tectonic environment following the collision and closure between the Songnen block and the Jiamusi block, which is correlated with the closure of the Mudanjiang Ocean. This also suggests that the amalgamation of the Songnen block and the Jiamusi block had already taken place during the late Early Jurassic period (177.2 Ma).

**Author Contributions:** Investigation, methodology, and writing—original draft preparation, J.K.; project administration and data curation, K.Q.; resources and writing—review and editing, X.H., L.Y., G.Z. and X.C. All authors have read and agreed to the published version of the manuscript.

**Funding:** This study was supported by the China Geological Survey Project (No. 1212011120342), the Liaoning Provincial Department of Science and Technology General Program (Nos. 20170540428 and 201601370), and the Liaoning Provincial Department of Education General Program (No. LJ2019JL027).

**Data Availability Statement:** The data that support the findings of this study are available from the corresponding author upon reasonable request.

**Acknowledgments:** We would like to sincerely thank the peer reviewers and the editorial team for their valuable and constructive comments on this paper. We also express our gratitude to the State Key Laboratory of Continental Dynamics at Northwest University and the Harbin Mineral Resources Supervision and Testing Center of the Ministry of Natural Resources for their support and assistance with the isotope-dating analysis and rock geochemical analysis experiments.

**Conflicts of Interest:** The authors declare no conflict of interest.

## References

1. Sengor, A.M.C.; Natal'in, B.A.; Burtman, V.S. Evolution of the Altaid tectonic collage and Palaeozoic crustal growth in Eurasia. *Nature* **1993**, *364*, 299–307. [[CrossRef](#)]
2. Wu, F.Y.; Sun, D.Y.; Li, H.M.; Jahn, B.M.; Wilde, S.A. A-Type granites in Northeastern China; age and geochemical constraints on their petrogenesis. *Chem. Geol.* **2002**, *187*, 143–173. [[CrossRef](#)]
3. Sengor, A.M.C.; Natal'in, B.A. Paleotectonics of Asia: Fragments of a synthesis. In *The Tectonic Evolution of Asia*; Yin, A., Harrison, M., Eds.; Cambridge University Press: London, UK, 1996; pp. 486–640.
4. Xu, W.L.; Ji, W.Q.; Pei, F.P.; Meng, E.; Yu, Y.; Yang, D.B.; Zhang, X.Z. Triassic volcanism in Eastern Heilongjiang and Jilin Provinces, NE China: Chronology, geochemistry, and tectonic implications. *J. Asian Earth Sci.* **2008**, *34*, 392–402. [[CrossRef](#)]
5. Wang, F.; Xu, W.L.; Gao, F.H.; Meng, E.; Cao, H.H.; Zhao, L.; Yang, Y. Tectonic history of the Zhangguangailing Group in eastern Heilongjiang Province, NE China: Constraints from U–Pb geochronology of detrital and magmatic zircons. *Tectonophysics* **2012**, *566–567*, 105–122. [[CrossRef](#)]
6. Zheng, W.; Yu, X.F. Geochronological and geochemical constraints on the petrogenesis and geodynamic setting of the Daheishan Porphyry Mo deposit, Northeast China. *Resour. Geol.* **2018**, *68*, 1–21. [[CrossRef](#)]
7. Xu, M.J.; Xu, W.L.; Wang, F.; Gao, F.H. Age, Association and Provenance of the “Neoproterozoic” Fengshuigouhe Group in the Northwestern Lesser Xing’an Range, NE China: Constraints from Zircon U–Pb Geochronology. *J. Earth Sci.* **2012**, *23*, 786–801. [[CrossRef](#)]
8. Duan, Z.P.; Jiang, S.Y.; Su, H.M.; Zhu, X.Y.; Zou, T.; Cheng, X.Y. Geochronological and geochemical investigations of the granites from the giant Shihuiyao Rb–(Nb–Ta–Be–Li) deposit, Inner Mongolia: Implications for magma source, magmatic evolution, and rare metal mineralization. *Lithos* **2021**, *400–401*, 106415. [[CrossRef](#)]

9. Yang, F.; Sun, J.G.; Wang, Y.; Fu, J.Y.; Na, F.C.; Fan, Z.Y.; Hu, Z.Z. Geology, Geochronology and Geochemistry of Weilasituo Sn-polymetallic Deposit in Inner Mongolia, China. *Minerals* **2019**, *9*, 104. [[CrossRef](#)]
10. Wu, F.Y.; Cao, L. Some important problems of geology in Northeastern Asia. *World Geol.* **1999**, *18*, 1–13. (In Chinese with English abstract)
11. Dong, Y.; Ge, W.C.; Yang, H.; Bi, J.H.; Wang, Z.H.; Xu, W.L. Permian tectonic evolution of the Mudanjiang Ocean: Evidence from zircon U–Pb–H isotopes and geochemistry of a N–S trending granitoid belt in the Jiamusi Massif, NE China. *Gondwana Res.* **2017**, *49*, 147–163. [[CrossRef](#)]
12. Liu, K.; Zhang, J.J.; Wilde, S.A.; Zhou, J.B.; Wang, M.; Ge, M.H.; Wang, J.M.; Ling, Y.Y. Initial subduction of the Paleo–Pacific Oceanic plate in NE China: Constraints from whole-rock geochemistry and zircon U–Pb and Lu–Hf isotopes of the Khanka Lake granitoids. *Lithos* **2017**, *274–275*, 254–270. [[CrossRef](#)]
13. Dong, Y. Convergence History of the Jiamusi and Songnen–Zhangguangcai Range Massifs: Geochronological and Geochemical Evidence. Ph.D. Thesis, Jilin University, Changchun, China, 2018. (In Chinese with English abstract)
14. Ge, M.H.; Zhang, J.J.; Li, L.; Liu, K. A Triassic–Jurassic westward scissor–like subduction history of the Mudanjiang Ocean and amalgamation of the Jiamusi Block in NE China: Constraints from whole-rock geochemistry and zircon U–Pb and Lu–Hf isotopes of the Lesser Xing’an–Zhangguangcai Range granitoids. *Lithos* **2018**, *302–303*, 263–277. [[CrossRef](#)]
15. Ge, M.H.; Zhang, J.J.; Li, L.; Liu, K.; Ling, Y.Y.; Wang, J.M.; Wang, M. Geochronology and geochemistry of the Heilongjiang Complex and the granitoids from the Lesser Xing’an–Zhangguangcai Range: Implications for the late Paleozoic–Mesozoic tectonics of eastern NE China. *Tectonophysics* **2017**, *717*, 565–584. [[CrossRef](#)]
16. Wu, F.Y.; Jahn, B.M.; Wilde, S.A.; Lo, C.H.; Yui, T.F.; Lin, Q.; Ge, W.C.; Sun, D.Y. Highly fractionated I type granites in NE China (I): Geochronology and petrogenesis. *Lithos* **2003**, *66*, 241–273. [[CrossRef](#)]
17. Wu, F.Y.; Jahn, B.M.; Wilde, S.A.; Lo, C.H.; Yui, T.F.; Lin, Q.; Ge, W.C.; Sun, D.Y. Highly fractionated I–type granites in NE China (II): Isotopic geochemistry and implications for crustal growth in the Phanerozoic. *Lithos* **2003**, *67*, 191–204. [[CrossRef](#)]
18. Wu, F.Y.; Jahn, B.M.; Wilde, S.A.; Sun, D.Y. Phanerozoic crustal growth: U–Pb and Sr–Nd isotopic evidence from the granites in northeastern China. *Tectonophysics* **2000**, *328*, 89–113. [[CrossRef](#)]
19. Jahn, B.; Windley, B.; Natal’in, B.; Dobretsov, N. Phanerozoic continental growth in Central Asia. *J. Asian Earth Sci.* **2004**, *23*, 599–603. [[CrossRef](#)]
20. Xu, W.L.; Pei, F.P.; Wang, F.; Meng, E.; Ji, W.Q.; Yang, D.B.; Wang, W. Spatial–temporal relationships of Mesozoic volcanic rocks in NE China: Constraints on tectonic overprinting and transformations between multiple tectonic regimes. *J. Asian Earth Sci.* **2013**, *74*, 167–193. [[CrossRef](#)]
21. Ma, X.H.; Cao, R.; Zhou, Z.H.; Zhu, W.P. Early Cretaceous high-Mg diorites in the Yanji area, northeastern China: Petrogenesis and tectonic implications. *J. Asian Earth Sci.* **2015**, *97*, 393–405. [[CrossRef](#)]
22. Yu, J.J.; Wang, F.; Xu, W.L.; Gao, F.H.; Pei, F.P. Early Jurassic mafic magmatism in the Lesser Xing’an–Zhangguangcai Range, NE China, and its tectonic implications: Constraints from zircon U–Pb chronology and geochemistry. *Lithos* **2012**, *142–143*, 256–266. [[CrossRef](#)]
23. Xu, M.J.; Xu, W.L.; Wang, F.; Gao, F.H.; Yu, J.J. Geochronology and geochemistry of the Early Jurassic granitoids in the central Lesser Xing’an Range, NE China and its tectonic implications. *Acta Petrol. Sin.* **2013**, *29*, 354–368. (In Chinese with English abstract)
24. Yin, Z.G.; Gong, Z.M.; Wang, C.S.; Liu, S.J.; Zhang, S.T.; Wang, G.Q.; Zhou, X.G.; Zhang, Z.H. Chronological, Geochemical Characteristics and Geological Significance of Early Jurassic Granites in Pingdingshan Area of Lesser Xing’an Range. *J. Jilin Univ. (Earth Sci. Ed.)* **2021**, *51*, 107–125. (In Chinese with English abstract)
25. Wu, F.Y.; Sun, D.Y.; Ge, W.C.; Zhang, Y.B.; Grant, M.L.; Wilde, S.A.; Jahn, B.M. Geochronology of the Phanerozoic granitoids in northeastern China. *J. Asian Earth Sci.* **2011**, *41*, 1–30. [[CrossRef](#)]
26. Ge, M.H.; Zhang, J.J.; Li, L.; Liu, K. Ages and geochemistry of Early Jurassic granitoids in the Lesser Xing’an–Zhangguangcai Ranges, NE China: Petrogenesis and tectonic implications. *Lithosphere* **2019**, *11*, 804–820. [[CrossRef](#)]
27. Ge, M.H.; Zhang, J.J.; Liu, K.; Wang, M.; Li, Z. Petrogenesis of the Late Paleozoic to Mesozoic granite from the Xiao Hinggan Mountains–Zhangguangcai Mountains and its geological implications. *Acta Petrol. Mineral.* **2020**, *39*, 385–405. (In Chinese, with English abstract)
28. Zhou, J.B.; Li, L. The Mesozoic accretionary complex in Northeast China: Evidence for the accretion history of Paleo–Pacific subduction. *J. Asian Earth Sci.* **2017**, *145*, 91–100. [[CrossRef](#)]
29. Feng, G.; Dilek, Y.; Niu, X.L.; Liu, F.; Yang, J.S. Geochemistry and geochronology of OIB–type, Early Jurassic magmatism in the Zhangguangcai range, NE China, as a result of continental back–arc extension. *Geol. Mag.* **2018**, *158*, 143–157. [[CrossRef](#)]
30. Zhu, C.Y.; Zhao, G.C.; Sun, M.; Eizenhöfer, P.R.; Han, Y.G.; Liu, Q.; Liu, X.D. Subduction between the Jiamusi and Songliao blocks: Geochronological and geochemical constraints from granitoids within the Zhangguangcailing orogen, northeastern China. *Lithosphere* **2017**, *9*, 515–533. [[CrossRef](#)]
31. Safonova, I.Y.; Santos, H.M. Accretionary complexes in the Asia–Pacific region: Tracing archives of ocean plate stratigraphy and tracking mantle plumes. *Gondwana Res.* **2014**, *25*, 126–158. [[CrossRef](#)]
32. Ryan, W.B.F.; Carbotte, S.M.; Coplan, J.O.; O’hara, S.; Melkonian, A.; Arko, R.; Weissel, R.A.; Ferrini, V.; Goodwillie, A.; Nitsche, F.; et al. Global multi–resolution topography synthesis. *Geochem. Geophys. Geosyst.* **2009**, *10*, 1–9. [[CrossRef](#)]

33. Griffin, W.L.; Pearson, N.J.; Belousova, E.A.; Saced, A. Comment Hf-isotope heterogeneity in standard zircon 91500. *Chem. Geol.* **2006**, *233*, 358–363. [[CrossRef](#)]
34. Liu, Y.S.; Gao, S.; Hu, Z.C.; Gao, C.G.; Zong, K.Q.; Wang, D.B. Continental and oceanic crust recycling-induced melt–peridotite interactions in the Trans-North China Orogen: U–Pb dating, Hf isotopes and trace elements in zircons of mantle xenoliths. *J. Petrol.* **2010**, *51*, 537–571. [[CrossRef](#)]
35. Ludwig, K.R. *User's Manual for Isoplot 3.0: A Geochronological Toolkit for Microsoft Excel*; Berkeley Geochronology Center: Berkeley, CA, USA, 2003; pp. 1–71.
36. Corfu, F.; Hanchar, J.M.; Hoskin, P.W.O.; Kinny, P. Atlas of zircon tetra- and octahedral site occupancies. *Rev. Mineral. Geochem.* **2003**, *53*, 469–500. [[CrossRef](#)]
37. Middlemost, E.A.K. Naming materials in the magma/igneous rock system. *Earth-Sci. Rev.* **1994**, *37*, 215–224. [[CrossRef](#)]
38. Wright, J.B.A. A simple alkalinity ratio and its application to questions of non-orogenic granite genesis. *Geol. Mag.* **1969**, *106*, 370–384. [[CrossRef](#)]
39. Maniar, P.D.; Piccoli, P.M. Tectonic discrimination of granitoids. *Geol. Soc. Am. Bull.* **1989**, *101*, 635–643. [[CrossRef](#)]
40. Sun, D.Y.; Wu, F.Y.; Gao, S.; Lu, X.P. Confirmation of two episodes of A-type granite emplacement during Late Triassic and Early Jurassic in the central Jilin Province, and their constraints on the structural pattern of Eastern Jilin-Heilongjiang Area, China. *Earth Sci. Front.* **2005**, *12*, 263–275. (In Chinese with English abstract)
41. Jiang, H.J. Characteristics and Geological Significance of the Mesozoic Granites of the New Second Forest Farm–Yuejin Forest Farm in Western Yichun. Master's Thesis, Chengdu University of Technology, Chengdu, China, 2020. (In Chinese with English abstract)
42. Zhao, Y.; Liu, J.D.; Zhang, G.B.; Zhang, Y.F. Geochronology, Geochemistry and Tectonic Significance of the Monzonitic Granites of Maoershan Pluton from the Southern Zhangguangcai Range in Heilongjiang Province. *China. J. Jilin Univ. (Earth Sci. Ed.)* **2021**, *51*, 1098–1118. (In Chinese with English abstract)
43. Ye, X.Q.; Sun, L.Y.; Xu, Z.T.; Yan, D.H.; Yang, Q.F.; Zhu, D.Q.; Feng, J.Q.; Chen, L.R. Geochemistry and zircon U–Pb dating of Early Jurassic syenogranite in the Kaoshan area, southern part of the Zhangguangcai Range, NE China, and tectonic implications. *Geol. J.* **2022**, *57*, 440–461. [[CrossRef](#)]
44. Ye, X.Q.; Sun, L.Y.; Xu, Z.T.; Yan, D.H.; Feng, J.Q.; Cao, R.J. Zircon U–Pb Geochronology, Geochemical Characteristics and Geodynamic Significance of the Early Jurassic Syenogranite in Kaoshan Area of Central Jilin Province. *J. Jilin Univ. (Earth Sci. Ed.)* **2023**, *53*, 964–983. (In Chinese with English abstract)
45. Zhang, G.B.; Chen, X.K.; Zhao, Y.; Tang, J.Y.; Li, R.R.; Feng, Y.; Kong, J.G. Geochronology, Geochemistry and Geological Significance of the Middle Jurassic Porphyritic Monzogranite in the Southern Zhangguangcai Range, Heilongjiang Province. *J. Jilin Univ. (Earth Sci. Ed.)* **2022**, *52*, 1907–1925, (in Chinese with English abstract).
46. Sun, S.S.; McDonough, W.F. Chemical and isotopic systematics of oceanic basalts: Implication mantle composition and processes. *Magmat. Ocean Basins Geol. Soc. Spec* **1989**, *42*, 313–345. [[CrossRef](#)]
47. Wang, F.; Xu, W.L.; Xu, Y.G.; Gao, F.H.; Ge, W.C. Late Triassic bimodal igneous rocks in eastern Heilongjiang Province, NE China: Implications for the initiation of subduction of the Paleo-Pacific Plate beneath Eurasia. *J. Asian Earth Sci.* **2015**, *97*, 406–423. [[CrossRef](#)]
48. Tang, J.; Xu, W.L.; Wang, F.; Gao, F.H.; Cao, H.H. Petrogenesis of bimodal volcanic rocks from Maoershan Formation in Zhangguangcai Range: Evidence from geochronology and geochemistry. *Glob. Geol.* **2011**, *30*, 508–520. (In Chinese with English abstract)
49. Miller, C.F. Are Strongly Peraluminous Magmas Derived from Pelitic Sedimentary Sources. *J. Geol.* **1985**, *93*, 673–689. [[CrossRef](#)]
50. Chappell, B.W.; White, A.J.R. I-Type and S-Type Granites in the Lachlan Fold Belt.—Transactions of the Royal Society of Edinburgh. *Earth Sci.* **1992**, *83*, 1–26. [[CrossRef](#)]
51. Whalen, J.B.; Currie, K.L.; Chappell, B.W. A-type granites: Geochemical characteristics, discrimination and petrogenesis. *Contrib. Mineral. Petrol.* **1987**, *95*, 407–419. [[CrossRef](#)]
52. Chappell, B.W. Aluminium saturation in I- and S-type granites and the characterization of fractionated haplogranites. *Lithos* **1999**, *46*, 535–551. [[CrossRef](#)]
53. Wu, F.Y.; Liu, X.C.; Ji, W.Q.; Wang, J.M.; Yang, G.L. Highly fractionated granites: Recognition and research. *Sci. China Earth Sci.* **2017**, *60*, 1201–1219. (In Chinese with English abstract) [[CrossRef](#)]
54. Turner, S.P.; Foden, J.D.; Morrison, R.S. Derivation of some A-type magmas by fractionation of basaltic magma: An example from the Pathway Ridge, South Australia. *Lithos* **1992**, *28*, 151–179. [[CrossRef](#)]
55. Green, T.H. Significance of Nb/Ta as an indicator of geochemical processes in the crust–mantle system. *Chem. Geol.* **1995**, *120*, 347–359. [[CrossRef](#)]
56. Chappell, B.W.; White, A.J.R. Two contrasting granite types: 25 years later. *Aust. J. Earth Sci.* **2001**, *48*, 489–499. [[CrossRef](#)]
57. Atherton, M.P.; Petford, N. Generation of Sodium-Rich Magmas from Newly Underplated Basaltic Crust. *Nature* **1993**, *362*, 144–146. [[CrossRef](#)]
58. Taylor, S.R.; McLennan, S.M. *The Continental Crust: I Composition and Evolution*; Blackwell Scientific Publication: Oxford, UK, 1985; p. 312.
59. Crawford, A.J.; Falloon, T.J.; Eggins, S. The Origin of Island Arc High-alumina Basalts. *Contrib. Mineral. Petrol.* **1987**, *97*, 417–430. [[CrossRef](#)]

60. Ozerov, A.Y. The Evolution of High-alumina Basalts of the Klyuchevskoy Volcano, Kamchatka, Russia, Based on Microprobe Analyses of Mineral Inclusions. *J. Volcanol. Geotherm. Res.* **2000**, *95*, 65–79. [[CrossRef](#)]
61. Douce, A.E.P. What do experiments tell us about the relative contributions of crust and mantle to the origin of granitic magmas? *Geol. Soc. Lond. Spec. Publ.* **1999**, *168*, 55–75. [[CrossRef](#)]
62. Wang, C.T.; Sun, D.Y.; Sun, R.J.; Gou, J.; Li, B. Geochemistry of Hengdaohezi Pluton from southern Zhangguangcai Range and its petrogenesis. *Glob. Geol.* **2015**, *34*, 321–329. (In Chinese with English abstract)
63. Li, H.N.; Han, J.; Zhao, Z.H.; Yin, Z.G. Magma-mixing origin for the Early Jurassic intrusive rocks in the eastern Songnen–Zhangguangcai Range Massif, NE China: Evidence from geochronology, geochemistry and Hf–O–Sr–Nd isotopes. *Gondwana Res.* **2023**, *121*, 72–91. [[CrossRef](#)]
64. Guo, F.; Li, H.X.; Fan, W.M.; Li, J.Y.; Zhao, L.; Huang, M.W.; Xu, W.L. Early Jurassic subduction of the Paleo–Pacific Ocean in NE China: Petrologic and geochemical evidence from the Tumen mafic intrusive complex. *Lithos* **2015**, *224*, 46–60. [[CrossRef](#)]
65. Sui, Z.M.; Ge, W.C.; Wu, F.Y.; Zhang, J.H.; Xu, X.C.; Cheng, R.Y. Zircon U–Pb ages, geochemistry and its petrogenesis of Jurassic granites in northwestern part of the Da Hinggan Mts. *Acta Petrol. Sin.* **2007**, *23*, 461–480. (In Chinese with English abstract)
66. Li, J.Y.; Guo, F.; Li, C.W.; Li, H.X.; Zhao, L. Neodymium isotopic variations of Late Paleozoic to Mesozoic I– and A–type granitoids in NE China: Implications for tectonic evolution. *Acta Petrol. Sin.* **2014**, *30*, 1995–2008. (In Chinese with English abstract)
67. Ren, R.; Han, B.F.; Xu, Z.; Zhou, Y.Z.; Liu, B.; Zhang, L.; Chen, J.F.; Su, L.; Li, J.; Li, X.H.; et al. When did the subduction first initiate in the southern Paleo-Asian Ocean: New constraints from a Cambrian intra-oceanic arc system in West Junggar, NW China. *Earth Planet. Sci. Lett.* **2014**, *388*, 222–236. [[CrossRef](#)]
68. Boztu, D.; Harlavan, Y.; Arel, G.B.; Satir, M.; Avci, N. K–Ar age, whole rock and isotope geochemistry of A type granitoids in the Divri-i&ndash;Sivas region, easterncentral Anatolia, Turkey. *Lithos* **2007**, *97*, 193–218. [[CrossRef](#)]
69. Pearce, J.A.; Bender, J.F.; De, S.E.; Kidd, W.S.F.; Low, P.J.; Güner, Y.; Saroglu, F.; Yilmaz, Y.; Moorbath, S.; Mitchell, J.G. Genesis of collision volcanism in Eastern Anatolia, Turkey. *J. Volcanol. Geotherm. Res.* **1990**, *44*, 189–229. [[CrossRef](#)]
70. Linnen, R.L.; Keppler, H. Melt composition control of Zr/Hf fractionation in magmatic processes. *Geochim. Cosmochim. Acta* **2002**, *66*, 3293–3301. [[CrossRef](#)]
71. Janoušek, V.; Finger, F.; Roberts, M.; Fryda, J.; Pin, C.; Dolejš, D. Deciphering the petrogenesis of deeply buried granites: Whole-rock geochemical constraints on the origin of largely undepleted felsic granulites from the Moldanubian Zone of the Bohemian Massif. *Earth Environ. Sci. Trans. R. Soc. Edinb.* **2004**, *95*, 141–159. [[CrossRef](#)]
72. Shao, J.A.; Li, Y.F.; Tang, K.D. Restoration of the orogenic processes of Zhangguangcai Range. *Acta Petrol. Sin.* **2013**, *29*, 2959–2970. (In Chinese with English abstract)
73. Wang, W.; Tang, J.; Xu, W.L.; Wang, F. Geochronology and geochemistry of Early Jurassic volcanic rocks in the Erguna Massif, northeast China: Petrogenesis and implications for the tectonic evolution of the Mongol–Okhotsk suture belt. *Lithos* **2015**, *218–219*, 73–86. [[CrossRef](#)]
74. Batchelor, R.A.; Bowden, P. Petrogenetic interpretation of granitoid rock series using m-ulticationic parameters. *Chem. Geol.* **1985**, *48*, 43–55. [[CrossRef](#)]
75. Wilde, S.A.; Zhou, J.B. The Late Paleozoic to Mesozoic evolution of the eastern margin of the Central Asian Orogenic Belt in China. *J. Asian Earth Sci.* **2015**, *113*, 909–921. [[CrossRef](#)]
76. Chen, C.; Ren, Y.S.; Zhao, H.L.; Yang, Q.; Shang, Q.Q. Age, tectonic setting, and metallogenic implication of Phanerozoic granitic magmatism at the eastern margin of the Xing’an–Mongolian Orogenic Belt, NE China. *J. Asian Earth Sci.* **2017**, *144*, 368–383. [[CrossRef](#)]
77. Chen, J.S.; Tian, D.X.; Yang, H.; Li, W.W.; Liu, M.; Li, B.; Yang, F.; Li, W.; Wu, Z. Tiassic granitic magmatism at the northern margin of the North China Craton: Implications of geochronology and geochemistry for the tectonic evolution of the Central Asian Orogenic Belt. *Acta Geologica Sinica.* **2019**, *93(5)*, 1325–1353. [[CrossRef](#)]
78. Yang, H.; Ge, W.C.; Zhao, G.C.; Yu, J.J.; Zhang, Y.L. Early Permian–Late Triassic granitic magmatism in the Jiamusi–Khanka Massif, eastern segment of the Central Asian Orogenic Belt and its implications. *Gondwana Res.* **2015**, *27*, 1509–1533. [[CrossRef](#)]
79. Zhu, C.Y.; Zhao, G.C.; Sun, M.; Liu, Q.; Han, Y.G.; Hou, W.Z.; Zhang, X.R.; Eizenhöfer, P.R. Geochronology and geochemistry of the Yilan blueschists in the Heilongjiang Complex, northeastern China and tectonic implications. *Lithos* **2015**, *216–217*, 241–253. [[CrossRef](#)]
80. Yang, D.G.; Sun, D.Y.; Guo, J.; Hou, X.G. U–Pb ages of zircons from Mesozoic intrusive rocks in the Yanbian area, Jilin Province, NE China: Transition of the Paleo–Asian oceanic regime to the circum–Pacific tectonic regime. *J. Asian Earth Sci.* **2017**, *143*, 171–190. [[CrossRef](#)]
81. Du, B.Y.; Liu, F.; Liu, Y.; Liu, Y.W.; Gao, H.Y.; Zhen, M.; Zhang, T.A. Permian–Early Jurassic ocean–Continent evolution and metallogenic dynamic setting in the central and eastern part of Heilongjiang Province. *Geol. Rev.* **2022**, *68*, 431–451. (In Chinese with English abstract)
82. Zhao, D.; Ge, W.C.; Yang, H.; Dong, Y.; Bi, J.H.; He, Y. Petrology, geochemistry, and zircon U–Pb–Hf isotopes of Late Triassic enclaves and host granitoids at the southeastern margin of the Songnen–Zhangguangcai Range Massif, Northeast China: Evidence for magma mixing during subduction of the Mudanjiang oceanic plate. *Lithos* **2018**, *312–313*, 358–374. [[CrossRef](#)]
83. Cheng, G.H.; Wang, R.L.; Zeng, Q.D.; Guo, Y.P.; Duan, X.X.; Wei, J.J.; Zhang, J.S.; Gao, X.H. Zircon U–Pb ages, Hf isotopes of the granitoids and Re–Os ages of the molybdenites in Luming molybdenum ore area, Heilongjiang Province, and its geological significance. *Acta Petrol. Sin.* **2015**, *31*, 2450–2464. (In Chinese with English abstract)

84. Fan, W.M.; Gup, F.; Gao, X.F.; Li, C.W. Sr–Nd isotope mapping of Mesozoic igneous rocks in NE China: Constraints on tectonic framework and crustal growth. *Geochimica* **2008**, *37*, 361–372. (In Chinese with English abstract)
85. Fei, X.; Zhang, Z.C.; Cheng, Z.G.; Santosh, M.; Jin, Z.L.; Wen, B.B.; Li, Z.X.; Xu, L.J. Highly differentiated magmas linked with polymetallic mineralization: A case study from the Cuihongshan granitic intrusions, Lesser Xing’an Range, NE China. *Lithos* **2018**, *302–303*, 158–177. [[CrossRef](#)]
86. Han, Z.Z.; Ren, X.; Schertl, H.P.; Li, X.P.; Song, Z.G.; Du, Q.X.; Han, C.; Zhong, W.J.; Gao, L.H. Zircon U–Pb–Hf isotopes and geochemistry of Jurassic igneous rocks from the southern Zhangguangcai Range, NE China: Constraints on magmatism, petrogenesis and tectonic implications. *Int. Geol. Rev.* **2019**, *62*, 1988–2012. [[CrossRef](#)]
87. Hao, B.W.; Luan, X.L.; Ge, L.S.; Zheng, X.L.; Xu, D.X.; Yang, S.H.; Li, X.; Cai, W.; Han, J.F. LA–CP–MS U–Pb Ages, Geochemical Features of the Dong’ an Alkali Feldspar Granites in Xunke County, Heilongjiang Province and Their Metallogenic Signification for the Mo–Pb–Zn–Polymetal Deposit. *Geol. Rev.* **2017**, *63*, 1664–1684. (In Chinese with English abstract)
88. Li, R. Age, Geochemistry and Petrogenesis of the Weihe Granite Batholith in the Northern Zhangguangcai Range. Master’s Thesis, Jilin University, Changchun, China, 2013. (In Chinese with English abstract)
89. Ouyang, H.G.; Mao, J.W.; Hu, R.Z.; Caulfield, J.; Zhou, Z.H. Controls on the metal endowment of porphyry Mo deposits: Insights from the Luming porphyry Mo deposit, northeastern China. *Econ. Geol.* **2021**, *116*, 1711–1735. [[CrossRef](#)]
90. Qin, J.F.; Lai, S.C.; Li, Y.F.; Ju, Y.J.; Zhu, R.Z.; Zhao, S.W. Early Jurassic monzogranite–tonalite association from the southern Zhangguangcai Range: Implications for paleo–Pacific plate subduction along northeastern China. *Lithosphere* **2016**, *8*, 396–411. [[CrossRef](#)]
91. Ren, Y.J. Early–Middle Jurassic granitic magmatism and tectonic evolution in the southern part of Zhangguangcai Range. *Acta Geol. Sin.* **2019**, *93*, 2813–2831. (In Chinese with English abstract)
92. Tang, J.; Xu, W.L.; Wang, F.; Ge, W.C. Subduction history of the Paleo–Pacific slab beneath Eurasian continent: Mesozoic–Paleogene magmatic records in Northeast Asia. *Sci. China Earth Sci.* **2018**, *61*, 527–559. (In Chinese with English abstract) [[CrossRef](#)]
93. Wang, N.; Zhang, Z.Y.; Malusà, M.G.; Wu, L.; Chew, D.; Zhang, J.; Xiang, D.F.; Xiao, W.J. Pulsed Mesozoic exhumation in Northeast Asia: New constraints from zircon U–Pb and apatite U–Pb, fission track and (U–Th)/He analyses in the Zhangguangcai Range, NE China. *Tectonophysics* **2021**, *818*, 229075. [[CrossRef](#)]
94. Wang, W.B.; Chen, G.H.; Wang, C.Z.; Zhu, R.Z.; Chen, J.W.; Ren, L.; Zheng, D.H. Early Jurassic granodiorite–monzogranite–granite suite in the Zhangguangcai Range, NE China: Implications for melting of newly accreted arc crust. *Geol. J.* **2022**, *57*, 1110–1124. [[CrossRef](#)]
95. Wei, H.Y.; Sun, D.Y.; Ye, S.Q.; Yang, Y.C.; Liu, Z.H.; Liu, X.M.; Hu, Z.C. Zircon U–Pb Ages and Its Geological Significance of the Granitic Rocks in the Yichun–Hegang Region, Southeastern Xiao Hinggan Mountains. *Earth Sci. J. China Univ. Geosci.* **2012**, *37*, 50–59. (In Chinese with English abstract)
96. Wu, F.Y.; Zhao, G.C.; Sun, D.Y.; Wilde, S.A.; Yang, J.H. The Hulan Group: Its role in the evolution of the Central Asian Orogenic Belt of NE China. *J. Asian Earth Sci.* **2007**, *30*, 542–556. [[CrossRef](#)]
97. Yang, C.J.; Wang, Y.C. LA–ICPMS zircon U–Pb age and the geological significance for Yichun Mesozoic granites in Southeast Lesser Khingan Range. *Jilin Geol.* **2010**, *29*, 1–5. (In Chinese with English abstract)
98. Zhang, L.S.; Sun, F.Y.; Li, B.L.; Qian, Y.; Zhang, Y.J.; Wang, L.; Wang, L.L. Petrogenesis and tectonic setting of granitoids in the Fu’anpu molybdenum deposit, Lesser Xing’an–Zhangguangcai range metallogenic belt: Constraints from element geochemistry, zircon U–Pb geochronology and Sr–Nd–Hf isotopes. *Acta Geol. Sin.* **2021**, *95*, 2471–2492. (In Chinese with English abstract)
99. Zhang, Y.B.; Wu, F.Y.; Wilde, S.A.; Zhai, M.G.; Lu, X.P.; Sun, D.Y. Zircon U–Pb ages and tectonic implications of “Early Paleozoic” granitoids at Yanbian, Jilin Province, northeast China. *Isl. Arc* **2004**, *13*, 484–505. [[CrossRef](#)]

**Disclaimer/Publisher’s Note:** The statements, opinions and data contained in all publications are solely those of the individual author(s) and contributor(s) and not of MDPI and/or the editor(s). MDPI and/or the editor(s) disclaim responsibility for any injury to people or property resulting from any ideas, methods, instructions or products referred to in the content.